# Coherence lengths in attractively interacting Fermi gases with spin-orbit coupling

Yu Yi-Xiang,[1,2] Jinwu Ye,[2,3] and Wu-Ming Liu[1]

[1]*Beijing National Laboratory for Condensed Matter Physics, Institute of Physics, Chinese Academy of Sciences, Beijing 100190, China*

[2]*Department of Physics and Astronomy, Mississippi State University, Mississippi State, Mississippi 39762, USA*

[3]*Key Laboratory of Terahertz Optoelectronics, Ministry of Education, Department of Physics, Capital Normal University, Beijing 100048, China*

(Received 27 August 2014; published 4 November 2014)

Extensive research has been lavished on the effects of spin-orbit couplings (SOCs) in attractively interacting Fermi systems in both neutral cold-atom systems and condensed-matter systems. Recently, it was suggested that a SOC drives a class of BCS to Bose-Einstein condensate (BEC) crossover that is different from the conventional one without a SOC. Here, we explore what are the most relevant physical quantities to describe such a BCS to BEC crossover and their experimental detections. We extend the concepts of the coherence length and "Cooper-pair size" in the absence of SOC to Fermi systems with SOC. We investigate the dependence of chemical potential, coherence length, and Cooper-pair size on the SOC strength and the scattering length at three dimensions (3D) (the bound-state energy at 2D) for three attractively interacting Fermi gases with 3D Rashba, 3D Weyl, and 2D Rashba SOC, respectively. We show that only the coherence length can be used to characterize this BCS to BEC crossover. Furthermore, it is the only length which can be directly measured by radio-frequency dissociation spectra type of experiments. We stress crucial differences among the coherence length, Cooper-pair size, and the two-body bound-state size. Our results provide the fundamental and global picture of the BCS to BEC crossover and its experimental detections in various cold-atom and condensed-matter systems.

DOI: 10.1103/PhysRevA.90.053603 PACS number(s): 03.75.Ss, 67.85.Lm, 71.70.Ej, 74.20.Fg

## I. INTRODUCTION

Spin-orbit coupling (SOC) has played important roles in various condensed-matter systems, such as anomalous Hall effects [1], noncentrosymmetric superconductors with lifted spin degeneracy [2], and exciton superfluids in electron-hole semiconductor bilayers [3,4]. Recently, the investigation and control of SOC have become subjects of intensive research after the discovery of the topological insulators [5,6]. For example, the SOC is a critical determining factor leading to an additional class of electronic states [7], such as various spin-orbital ordered states, spin liquids, various topological phases, etc. The one-dimensional (1D) SOC which is a linear combination of Rashba and Dresselhauss SOC has been successfully generated in several experimental groups for neutral atoms both in Bose and Fermi gas [8–11]. Possible experimental constructions of 2D Rashba or Dresselhauss SOC and 3D Weyl SOC have also been proposed [12,13]. There are also extensive theoretical investigations on various important effects of SOC on attractively interacting [14–17] degenerate Fermi gases across BCS to Bose-Einstein condensate (BEC) crossover. Collective excitations above the mean-field states have also been calculated in [18–21]. The collective modes and magnetic transitions in repulsively interacting Fermi gas have been investigated [22,23]. Recently, both staggered [24] and uniform [25] artificial magnetic fields have been generated in optical lattices. Scaling functions for various gauge-invariant and non-gauge-invariant quantities across topological transitions driven by the SOC on an optical lattice have been derived [26]. In particular, it was also stressed in [26] that in contrast to condensed-matter experiments where only gauge-invariant quantities can be measured, both gauge-invariant and non-gauge-invariant quantities can be measured by experimentally generating various non-Abelian gauges corresponding to the same set of Wilson loops. The interplay among the SOC, interactions, and lattice geometries leading to a different quantum phase, excitation spectrum, and quantum phase transitions has also been explored [27].

The BCS to BEC crossover is a longstanding problem in both condensed matter [28,29] and cold atoms [30]. Conventional superconductors are well inside the BCS limit, so mean-field theory works well [28,29]. Due to its short coherence $\xi$, high-temperature superconductors are near the BCS to BEC crossover, but still in the BCS side with a well-defined Fermi surface [29,31], so quantum fluctuation effects are large. The BCS to BEC crossover of exciton superfluids in an electron-hole semiconductor bilayer can be tuned by the exciton density [32–35]. The BCS to BEC crossovers of attractively interacting neutral fermions are tuned by sweeping across a Feshbach resonance [30]. The effects of SOC on the BCS to BEC crossover have been investigated by several groups [14–17]. In particular, the authors in [15] found that when the SOC strength is well beyond the value of the topological Lifshitz transition of the noninteracting Fermi surfaces [23,26], the overlap between the two-body wave function [14,28] and the "Cooper-pair wave function" [36] (see Sec. II B for its definition) approaches 1. So they concluded that at a fixed scattering length at the BCS side (in the absence of SOC), the SOC drives a BCS to BEC crossover which is in a different class than the one without a SOC driven by the exciton density [32–35] or Feshbach resonance [30]. However, as shown in this paper, the Cooper-pair wave function is useful for illustration purposes only instead of being physical, so its overlap with the two-body wave function is not physical and cannot be measured experimentally. In order to describe the SOC-driven BCS to BEC crossover, it is important to identify and compute the most relevant physical quantity to describe such a BCS to BEC crossover and then address its experimental detections.

 

In this paper, we address this outstanding problem by investigating three spin-orbit-coupled Fermi gases: (1) a 3D Fermi gas with a Rashba SOC, (2) a 3D Fermi gas with a isotropic Weyl SOC, and (3) a 2D Fermi gas with a Rashba SOC. We first extend the concepts of the coherence length associated with a many-body wave function [28,29,37] and "Cooper-pair size" [36] associated with a Cooper-pair wave function in the absence of SOC to Fermi systems with a SOC. The three systems have different symmetries: the $[\mathrm{U}(1)_{\mathrm{spin}} \times \mathrm{U}(1)_{\mathrm{orbit}}]_D$ symmetry at 3D where the $D$ means the spontaneous rotation in spin and orbital space, the $[\mathrm{SU}(2)_{\mathrm{spin}} \times \mathrm{SO}(3)_{\mathrm{orbit}}]_D$ symmetry at 3D, and the $[\mathrm{U}(1)_{\mathrm{spin}} \times \mathrm{U}(1)_{\mathrm{orbit}}]_D$ symmetry at 2D, respectively. These symmetries determine the number of independent coherence lengths and Cooper-pair sizes to be 2, 1, and 1, respectively. We then study the dependence of chemical potential, coherence length, and Cooper-pair size on the SOC strength $\lambda$ for three attractively interacting Fermi gases. We show that from the BCS side at $\lambda = 0$, as the SOC strength increases, the chemical potential drops below the bottom of the single-particle spectrum $\mu_0 = -\frac{\lambda^2}{2m}$, so it can be used to qualitatively characterize the BCS to BEC crossovers driven by the SOC strength. The coherence length decreases monotonically and quickly below the interparticle spacing, and so it can be used to quantitatively characterize the BCS to BEC crossovers. Furthermore, the coherence length can be directly measured by using radio-frequency dissociation spectra type of experiments [38] as soon as the 2D and 3D SOC can be realized experimentally. In sharp contrast, the Cooper-pair size used in the previous work [14–16] shows nonmonotonic behaviors, so it may not be used to characterize the BCS to BEC crossover even qualitatively. Furthermore, it is not an experimentally measurable quantity. Starting from the BEC side at $\lambda = 0$, the effects of SOC are small; both the coherence length and the Cooper-pair size converge to the two-body bound-state size [14,28]. We conclude that the coherence length is a much more robust concept than the Cooper-pair size; it is also the only experimentally detectable physical quantity which can be used to describe the BCS to BEC crossover even quantitatively. We also discuss relations among the many-body BCS wave functions, the Cooper-pair wave functions, and the two-body wave functions, and therefore stress crucial differences among the coherence length, Cooper-pair size, and the two-body bound-state size. The results provide a solid foundation for the fundamental physics of the SOC-driven BCS to BEC crossover and its experimental detections. Our results should also shed considerable light on condensed-matter systems such as 2D exciton superfluids and 2D noncentrosymmetric superconductors.

The rest of the paper is organized as follows: In Sec. II, we first review the different definitions and concepts of coherence length and Cooper-pair size, then extend these concepts to a SOC system where the spin is not a conserved quantity. In Sec. III, for a 3D Rashba system, we study how the chemical potential, the coherence length, and the Cooper-pair size change as the SOC strength increases, and we especially focus on their behaviors across the SOC-driven BCS to BEC crossover driven by the SOC strength. To be complete, we also study how the the coherence length and the Cooper-pair size change with the scattering lengths at fixed SOC strengths. We also discuss the crucial differences among the coherence length, Cooper-pair size, and two-body bound-state size. In Sec. IV, we compute the same quantities on 3D Fermi gas with an isotropic Weyl SOC. In Sec. V, we perform similar calculations on 2D Fermi gas with Rashba SOC, which needs a different regularization than the two 3D systems discussed in the previous two sections. In Sec. VI, we discuss the implications of the results achieved in the previous sections, especially in Sec. V, on several condensed-matter systems. We summarize the main results and discuss several exciting perspectives in Sec. VII. In the following and also in all the figures, we set $\hbar = 1$.

## II. EXTEND PAIRING LENGTH AND COOPER-PAIR SIZE TO SOC SYSTEMS

We consider a homogeneous Fermi gas with an attractive contact potential,

$$H = \sum_{\boldsymbol{p},\sigma=\uparrow,\downarrow} c^\dagger_{\boldsymbol{p}\sigma}\left(\frac{\boldsymbol{p}^2}{2m} - \mu\right) c_{\boldsymbol{p}\sigma} + V_{\mathrm{soc}} + \frac{g}{V}\sum_{\boldsymbol{p},\boldsymbol{q},s} c^\dagger_{\frac{s}{2}+\boldsymbol{p}\uparrow} c^\dagger_{\frac{s}{2}-\boldsymbol{p}\downarrow} c_{\frac{s}{2}-\boldsymbol{q}\downarrow} c_{\frac{s}{2}+\boldsymbol{q}\uparrow}, \tag{1}$$

where $d = 2,3$, and $V_{\mathrm{soc}}$ is the spin-orbit coupling (SOC) term which can be Rashba type, $-i\lambda(\partial_x\sigma_x + \partial_y\sigma_y)$, or a 3D Weyl isotropic SOC, $\lambda\vec{k}\cdot\vec{\sigma}$.

It is known that the interaction $g$ needs to be regularized differently in 2D and 3D. In 3D, the $g$ can be regularized by the $s$-wave scattering length $a_s$: $\frac{1}{g} = \frac{m}{4\pi a_s} - \frac{1}{V}\sum_{\boldsymbol{p}}\frac{1}{2\epsilon_{\boldsymbol{p}}}$ where $V$ is the volume of the system and $\epsilon_{\boldsymbol{p}} = \frac{\boldsymbol{p}^2}{2m}$ is the free-particle dispersion. In 2D, the $g$ can be regularized by the two-body binding energy $\epsilon_B$: $\frac{1}{g} = -\frac{1}{V}\sum_{\boldsymbol{p}}\frac{1}{2\epsilon_{\boldsymbol{p}}+\epsilon_B}$.

By introducing the order parameter $\Delta = \frac{g}{V}\sum_{\boldsymbol{p}}\langle c_{-\boldsymbol{p}\downarrow}c_{\boldsymbol{p}\uparrow}\rangle$, one can reduce the interaction term to the mean-field form: $H^{\mathrm{MF}}_{\mathrm{int}} = \sum_{\boldsymbol{p}}(\Delta^* c_{-\boldsymbol{p}\downarrow}c_{\boldsymbol{p}\uparrow} + \Delta c^\dagger_{\boldsymbol{p}\uparrow}c^\dagger_{-\boldsymbol{p}\downarrow}) - \frac{V|\Delta|^2}{g}$. The chemical potential $\mu$ and the order parameter $\Delta$ can be determined by two self-consistent equations: the number equation $n = \frac{1}{V}\sum_{\boldsymbol{p},\sigma}\langle c^\dagger_{\boldsymbol{p}\sigma}c_{\boldsymbol{p}\sigma}\rangle_{\mathrm{MF}}$ and the gap equation $\Delta = \frac{g}{V}\sum_{\boldsymbol{p}}\langle c_{-\boldsymbol{p}\downarrow}c_{\boldsymbol{p}\uparrow}\rangle_{\mathrm{MF}}$.

Without SOC, the coherence length has been calculated in Fermi gas across the whole BCS to BEC crossover tuned by Feshbach resonance in [37]. Most importantly, it has been measured using radio-frequency dissociation spectra throughout the whole BCS to BEC crossover in [38]. However, the effects of SOC on the pairing correlation lengths have not been studied. In this section, we first review the definition and concepts of the coherence length without SOC, then extend to the SOC case.

### A. Coherence length

For a spin-singlet superfluid without SOC, the fermion pair correlation functions are defined as

$$\psi(\vec{r}) = \frac{1}{n^2}\langle c^\dagger_\uparrow(\vec{r})c^\dagger_\downarrow(0)c_\downarrow(0)c_\uparrow(\vec{r})\rangle - \frac{1}{4}, \tag{2}$$

where $n$ is the particle density and the average is taken with respect to the BCS ground state $|\Phi\rangle = |\mathrm{BCS}\rangle$ (in the second

quantized form),

$$|\Phi\rangle = \Pi_{\vec{k}}(u_{\vec{k}} + v_{\vec{k}} c^{\dagger}_{\vec{k}\uparrow} c^{\dagger}_{-\vec{k}\downarrow})|0\rangle$$
$$= (\Pi_{\vec{k}} u_{\vec{k}})\Pi_{\vec{k}} \left(1 + \frac{v_{\vec{k}}}{u_{\vec{k}}} c^{\dagger}_{\vec{k}\uparrow} c^{\dagger}_{-\vec{k}\downarrow}\right)|0\rangle$$
$$= (\Pi_{\vec{k}} u_{\vec{k}}) \exp\left[\sum_{\vec{k}} \frac{v_{\vec{k}}}{u_{\vec{k}}} c^{\dagger}_{\vec{k}\uparrow} c^{\dagger}_{-\vec{k}\downarrow}\right]|0\rangle, \quad (3)$$

which obviously hosts an indefinite number of fermions. Its first quantized form was discussed in [28].

The coherence length is defined as [37,38]

$$\xi_c^2 = \frac{\int d\vec{r}\,\psi(\vec{r}) r^2}{\int d\vec{r}\,\psi(\vec{r})}. \quad (4)$$

At the mean-field level, Eq. (2) reduces to

$$\psi(\vec{r}) = \frac{1}{n^2} |\langle \Phi | c^{\dagger}_{\uparrow}(\vec{r}) c^{\dagger}_{\downarrow}(0) | \Phi \rangle|^2, \quad (5)$$

where $|\Phi\rangle = |\mathrm{BCS}\rangle$.

Under the mean-field approximation, Eq. (4) can be rewritten as [38]

$$\xi_c^2 = \frac{\langle \psi_{\alpha\beta} | r^2 | \psi_{\alpha\beta} \rangle}{\langle \psi_{\alpha\beta} | \psi_{\alpha\beta} \rangle}, \quad (6)$$

where $\psi_{\alpha\beta}(\vec{r}) = \langle \Phi | c^{\dagger}_{\alpha}(\vec{r}) c^{\dagger}_{\beta}(0) | \Phi \rangle$ with $\alpha = \uparrow, \beta = \downarrow$.

The Fourier transform of Eq. (6) to $\vec{k}$ space leads to

$$\xi_c^2 = \frac{\langle \psi_{\alpha\beta} | \nabla^2_{\vec{k}} | \psi_{\alpha\beta} \rangle}{\langle \psi_{\alpha\beta} | \psi_{\alpha\beta} \rangle}, \quad \alpha = \uparrow, \beta = \downarrow, \quad (7)$$

where $\psi_{\alpha\beta}(\vec{k}) = \langle \Phi | c^{\dagger}_{\alpha}(\vec{k}) c^{\dagger}_{\beta}(-\vec{k}) | \Phi \rangle$ is the Fourier transform of $\psi_{\alpha\beta}(\vec{r})$ with $\alpha = \uparrow, \beta = \downarrow$. More straightforwardly, Eq. (6) in real space and Eq. (7) in momentum space are Fourier transformed to each other.

For a BEC to BCS crossover without SOC, the only pairing is the singlet pairing so $\psi_{\uparrow\downarrow}(\vec{k}) = \langle \Phi | c^{\dagger}_{\uparrow}(\vec{k}) c^{\dagger}_{\downarrow}(-\vec{k}) | \Phi \rangle = u_{\vec{k}} v_{\vec{k}} = \frac{\Delta_0}{2E_{\vec{k}}}$, which is given and shown in Fig. 3 in [37].

It is important to point out that Eqs. (2) and (4) hold in general, while Eqs. (5) and (6) hold only at the mean-field level. Only at the mean-field level can one "intuitively" interpret Eqs. (5) and (6) as the expectation value of $r^2$ over the "pairing wave function" $\psi_{\alpha\beta}(\vec{r}) = \langle \Phi | c^{\dagger}_{\alpha}(\vec{r}) c^{\dagger}_{\beta}(0) | \Phi \rangle$ with $\alpha = \uparrow, \beta = \downarrow$. Although the concept of coherence length given by Eq. (4) holds in general, such a wave-function interpretation breaks down beyond the mean field.

In the presence of SOC, due to the nonconservation of spins, one needs to average over all the spin components to define the fermion pair correlation functions; so Eq. (2) should be replaced by

$$\psi(\vec{r}) = \frac{1}{n^2} \sum_{\alpha,\beta} \langle c^{\dagger}_{\alpha}(\vec{r}) c^{\dagger}_{\beta}(0) c_{\beta}(0) c_{\alpha}(\vec{r}) \rangle - 1, \quad (8)$$

where $n$ is the particle density. Equation (4) remains.

At the mean-field level, following the steps to derive Eqs. (5) and (6) leads to the coherence length in the presence of SOC,

$$\xi_i^2 = \frac{\sum_{\vec{k},\alpha,\beta} \langle \psi_{\alpha\beta} | \partial^2_{k_i} | \psi_{\alpha\beta} \rangle}{\sum_{\vec{k},\alpha,\beta} \langle \psi_{\alpha\beta} | \psi_{\alpha\beta} \rangle}, \quad \alpha, \beta = \uparrow, \downarrow, \quad (9)$$

which could be measured by radio-frequency dissociation spectra used in the experiment [38] in the presence of SOC. After the spin sum, the orbital symmetry of the $\mathrm{U(1)_{orbit}}$,$\mathrm{O(3)_{orbit}}$,$\mathrm{U(1)_{orbit}}$ of the three systems to be discussed in the following three sections will be recovered. However, one still needs to distinguish the pairing correlation length within the $xy$ plane and along the $z$ direction, $\xi^2_{xy} \neq \xi^2_z$, in the first and third systems.

### B. Cooper-pair size

In fact, one can also define the Cooper-pair size through the Cooper-pair wave function [28,39]. Removing the exponential in the normalized BCS wave function without SOC in Eq. (3) leads to the singlet Cooper-pair wave function in the second quantized form,

$$|g_{cp}\rangle = \sum_{\vec{k}} \frac{v_{\vec{k}}}{u_{\vec{k}}} c^{\dagger}_{\vec{k}\uparrow} c^{\dagger}_{-\vec{k}\downarrow} |0\rangle, \quad (10)$$

which hosts only two paired fermions. It can be understood as the two electron components of the many-body wave function.

One can extract the Cooper-pair wave function in the real space in the first quantization,

$$g_{cp}(\vec{r}) = g_{\uparrow\downarrow}(\vec{r})(|\uparrow\downarrow\rangle - |\downarrow\uparrow\rangle), \quad g_{\uparrow\downarrow}(\vec{r}) = \sum_{\vec{k}} e^{i\vec{k}\cdot\vec{r}} \frac{v_{\vec{k}}}{u_{\vec{k}}}. \quad (11)$$

It is necessary to point out that this Cooper-pair wave function is different from the original pairing problem of two fermions near a Fermi surface first achieved by Cooper by solving the Schrödinger equation [28].

The Cooper-pair size [36] is defined by [28,39]

$$l^2_{\mathrm{pair}} = \frac{\int d\vec{r} |g_{\uparrow\downarrow}(\vec{r})|^2 r^2}{\int d\vec{r} |g_{\uparrow\downarrow}(\vec{r})|^2} = \frac{\langle g_{cp} | r^2 | g_{cp} \rangle}{\langle g_{cp} | g_{cp} \rangle}. \quad (12)$$

The Fourier transform of Eq. (12) to $\vec{k}$ space leads to

$$l^2_{\mathrm{pair}} = \frac{\langle g_{\alpha\beta} | \nabla^2_{\vec{k}} | g_{\alpha\beta} \rangle}{\langle g_{\alpha\beta} | g_{\alpha\beta} \rangle}, \quad \alpha = \uparrow, \beta = \downarrow, \quad (13)$$

where $g_{\uparrow\downarrow}(\vec{k}) = \frac{v_{\vec{k}}}{u_{\vec{k}}}$ is the Fourier transform of $g_{\uparrow\downarrow}(\vec{r})$. This should be contrasted with $\psi_{\uparrow\downarrow}(\vec{k}) = \langle \Phi | c^{\dagger}_{\uparrow}(\vec{k}) c^{\dagger}_{\downarrow}(-\vec{k}) | \Phi \rangle = u_{\vec{k}} v_{\vec{k}} = \frac{\Delta_0}{2E_{\vec{k}}}$ used in Eq. (7).

It is important to point out that Eqs. (3) and (11)–(13) hold only in the mean-field level. Only at the mean-field level can one intuitively interpret Eqs. (12) and (13) as the expectation value of $r^2$ over the Cooper-pair wave function given by Eq. (11). However, the concept of Cooper-pair size, given by Eq. (13), breaks down beyond the mean-field theory.

In the presence of SOC, after writing the mean-field ground state in the form $|\mathrm{BCS}\rangle_{\mathrm{SOC}} \propto \exp[\sum_{\vec{k}} g_{\alpha\beta}(\vec{k}) c^{\dagger}_{\vec{k}\alpha} c^{\dagger}_{-\vec{k}\beta}]|0\rangle$, one

can extract the Cooper-pair size [28,39] as

$$l_i^2 = \frac{\sum_{\vec{k},\alpha,\beta}\langle g_{\alpha\beta}|\partial_{k_i}^2|g_{\alpha\beta}\rangle}{\sum_{\vec{k},\alpha,\beta}\langle g_{\alpha\beta}|g_{\alpha\beta}\rangle}, \quad \alpha,\beta=\uparrow,\downarrow, \tag{14}$$

where the average over all the spin components is performed. Note that $g_{\alpha\beta}(\vec{k})$ is very different from $\phi_{\alpha\beta}(\vec{k})$, so we may expect quite different behaviors from the two lengths. These will be explicitly demonstrated in the following sections. It is the coherence length which is measured in [38].

In the following, we apply the formalism to the 3D Rashba SOC, 3D Weyl SOC, and 2D Rashba SOC systems.

## III. 3D FERMI GAS WITH A RASHBA SOC

The 3D Rashba SOC $V_{3D-ra} = -i\lambda(\partial_x\sigma_x + \partial_y\sigma_y)$ can be written in the second quantization form,

$$V_{3D-ra} = \frac{\lambda}{m}\sum_{\boldsymbol{p}} p_\perp[e^{-i\varphi_{\boldsymbol{p}}}c^\dagger_{\boldsymbol{p}\uparrow}c_{\boldsymbol{p}\downarrow} + e^{i\varphi_{\boldsymbol{p}}}c^\dagger_{\boldsymbol{p}\downarrow}c_{\boldsymbol{p}\uparrow}], \tag{15}$$

where $\lambda$ is the SOC strength, $p_\perp = \sqrt{p_x^2+p_y^2}$, and $\varphi_{\boldsymbol{p}} = \mathrm{Arg}(p_x + ip_y)$. Note that in some references, the Rashba SOC was written as $V_{3D-ra} = -i\lambda(\partial_x\sigma_y - \partial_y\sigma_x)$. In fact, both forms are equivalent under the global $\frac{\pi}{2}$ rotation around the spin $z$ axis, $c_\sigma \to e^{-i\pi/4\sigma_z}c_\sigma$. It is easy to see that under this rotation, $(\sigma_x,\sigma_y,\sigma_z) \to (\sigma_y,-\sigma_x,\sigma_z)$, so the two forms transform to each other. The Dresselhauss SOC can be written as $V_{3D-D} = -i\lambda(\partial_x\sigma_x - \partial_y\sigma_y)$. Under the same rotation, it becomes $V_{3D-D} = -i\lambda(\partial_x\sigma_y + \partial_y\sigma_x)$. Then one needs to change $\varphi_{\boldsymbol{p}} \to -\varphi_{\boldsymbol{p}}$ in Eq. (15). We find that the final results on the coherence length, Cooper-pair size, and two-body bound state stay the same as those in the Rashba SOC case. So, in the following, we only focus on the Rashba SOC.

This model has been studied by previous works [16,17] with different focuses. The single-particle part $H_0$ in the Hamiltonian given by Eq. (1) can be diagonalized in the helicity base as

$$H_0 = \sum_{\boldsymbol{p}}(\xi_{\boldsymbol{p}+}h^\dagger_{\boldsymbol{p}+}h_{\boldsymbol{p}+} + \xi_{\boldsymbol{p}-}h^\dagger_{\boldsymbol{p}-}h_{\boldsymbol{p}-}), \tag{16}$$

where $\xi_{\boldsymbol{p}\pm} = \frac{p^2}{2m} \pm \frac{\lambda p_\perp}{m} - \mu$ and the two helicity operators are

$$\begin{aligned} h_{\boldsymbol{p}+} &= [c_{\boldsymbol{p}\uparrow} + e^{-i\varphi_{\boldsymbol{p}}}c_{\boldsymbol{p}\downarrow}]/\sqrt{2}, \\ h_{\boldsymbol{p}-} &= [e^{i\varphi_{\boldsymbol{p}}}c_{\boldsymbol{p}\uparrow} - c_{\boldsymbol{p}\downarrow}]/\sqrt{2}. \end{aligned} \tag{17}$$

In the helicity base, the mean-field interaction can be rewritten as $H_{\mathrm{int}}^{\mathrm{MF}} = -\frac{1}{2}\sum_{\boldsymbol{p}}(\Delta_0 e^{-i\varphi_{\boldsymbol{p}}}h^\dagger_{\boldsymbol{p}+}h^\dagger_{-\boldsymbol{p}+} + \Delta_0 e^{i\varphi_{\boldsymbol{p}}}h^\dagger_{\boldsymbol{p}-}h^\dagger_{-\boldsymbol{p}-} + \mathrm{H.c.}) - \frac{V|\Delta|^2}{g}$. The total Hamiltonian $H = H_0 + H_{\mathrm{int}}^{\mathrm{MF}}$ can be diagonalized by a Bogoliubov transformation,

$$\begin{aligned} H = &\sum_{\boldsymbol{p}}(E_{\boldsymbol{p}+}\alpha^\dagger_{\boldsymbol{p}+}\alpha_{\boldsymbol{p}+} + E_{\boldsymbol{p}-}\alpha^\dagger_{\boldsymbol{p}-}\alpha_{\boldsymbol{p}-}) \\ &- \sum_{\boldsymbol{p}}\frac{E_{\boldsymbol{p}+}+E_{\boldsymbol{p}-}}{2} - \frac{V|\Delta_0|^2}{g}, \end{aligned} \tag{18}$$

where the quasiparticle excitation energy $E_{\boldsymbol{p}\pm} = \sqrt{\xi^2_{\boldsymbol{p}\pm} + |\Delta_0|^2}$, and the quasiparticle operators

$$\begin{aligned} \alpha_{\boldsymbol{p}+} &= \sqrt{\frac{E_{\boldsymbol{p}+}+\xi_{\boldsymbol{p}+}}{2E_{\boldsymbol{p}+}}}e^{i\varphi_{\boldsymbol{p}}}h_{\boldsymbol{p}+} - \sqrt{\frac{E_{\boldsymbol{p}+}-\xi_{\boldsymbol{p}+}}{2E_{\boldsymbol{p}+}}}h^\dagger_{-\boldsymbol{p}+}, \\ \alpha_{\boldsymbol{p}-} &= \sqrt{\frac{E_{\boldsymbol{p}-}+\xi_{\boldsymbol{p}-}}{2E_{\boldsymbol{p}-}}}e^{-i\varphi_{\boldsymbol{p}}}h_{\boldsymbol{p}-} - \sqrt{\frac{E_{\boldsymbol{p}-}-\xi_{\boldsymbol{p}-}}{2E_{\boldsymbol{p}-}}}h^\dagger_{-\boldsymbol{p}-}, \end{aligned} \tag{19}$$

where all anticommutation relations hold ($\{\alpha_{\boldsymbol{p}+},\alpha^\dagger_{\boldsymbol{p}+}\} = 1$, $\{\alpha_{\boldsymbol{p}+},\alpha^\dagger_{\boldsymbol{p}-}\} = 0$, and so on).

At zero temperature, the two self-consistent equations become

$$\begin{aligned} n &= \frac{1}{V}\sum_{\boldsymbol{p}}\left[1 - \frac{\xi_{\boldsymbol{p}+}}{2E_{p+}} - \frac{\xi_{\boldsymbol{p}-}}{2E_{p-}}\right], \\ \frac{1}{g} &= -\frac{1}{4V}\sum_{\boldsymbol{p}}\left[\frac{1}{E_{p+}} + \frac{1}{E_{p-}}\right], \end{aligned} \tag{20}$$

where, as said in Sec. II, the interaction strength $g$ can be regularized by the $s$-wave scattering length $a_s$: $\frac{1}{g} = \frac{m}{4\pi a_s} - \frac{1}{V}\sum_{\boldsymbol{p}}\frac{1}{2\epsilon_{\boldsymbol{p}}}$. In the rest of the section, we will determine the chemical potential $\mu$, the pairing length $\xi_i$ in Eq. (9), and the Cooper-pair size $l_i$ in Eq. (14). Finally, we will compare our many-body results with the corresponding two-body results [14].

### A. Chemical potential across BCS to BEC crossover

One can find the chemical potential $\mu$ by solving Eq. (20). It is shown in Fig. 1. As a contrast, the minimum of the single-

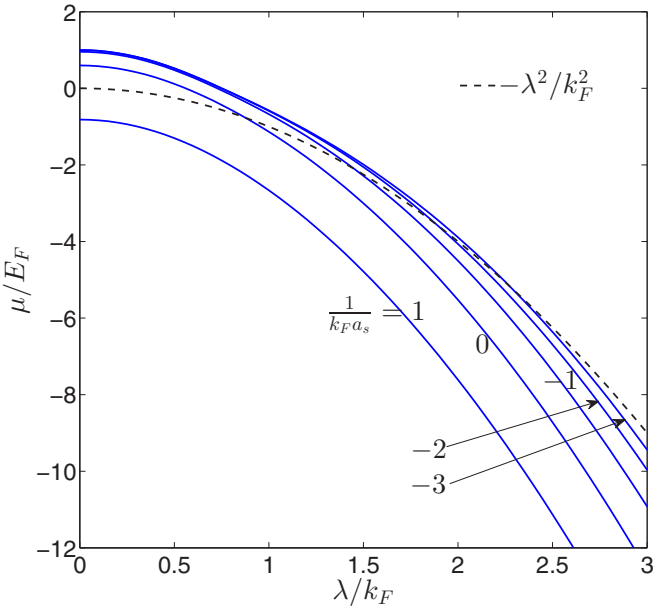


FIG. 1. (Color online) The chemical potential $\mu$ vs $\lambda$ in a 3D Rashba SOC for different scattering lengths. The dashed line is the bottom of the single-particle spectrum $\mu_0 = -\frac{\lambda^2}{2m}$. Starting from the BCS side at $\lambda = 0$, as $\lambda$ increases, the $\mu$ drops below $\mu_0$. This fact indicates that the system evolves into the BEC state.

particle excitation energy $\mu_0 = \mathrm{Min}_{\boldsymbol{p}}\{\frac{p^2}{2m} - \frac{\lambda p_\perp}{m}\} = -\frac{\lambda^2}{2m}$ is also plotted in Fig. 1. We can qualitatively assign the region with $\mu > \mu_0$ as the BCS region and $\mu < \mu_0$ as the BEC region. As shown in Fig. 1, starting from the BCS side at $\lambda = 0$, as $\lambda$ increases, the $\mu$ drops below $\mu_0$. Therefore, we conclude that Rashba SOC can drive a crossover from BCS to BEC, as first pointed out in [15].

### B. Coherence length across BCS to BEC crossover

The BCS ground state can be written as

$$|\mathrm{BCS}\rangle = \prod_{\boldsymbol{p}}{}' \alpha_{\boldsymbol{p}+}\alpha_{-\boldsymbol{p}+}\alpha_{\boldsymbol{p}-}\alpha_{-\boldsymbol{p}-}|0\rangle \propto \exp\sum_{\boldsymbol{p}}{}' [w_{\boldsymbol{p}+}e^{-i\varphi_{\boldsymbol{p}}}h^\dagger_{\boldsymbol{p}+}h^\dagger_{-\boldsymbol{p}+} + w_{\boldsymbol{p}-}e^{i\varphi_{\boldsymbol{p}}}h^\dagger_{\boldsymbol{p}-}h^\dagger_{-\boldsymbol{p}-}]|0\rangle, \tag{21}$$

where the $'$ means half of the momentum space and $|0\rangle$ is the electron vacuum state and $w_{\boldsymbol{p}\pm} = \sqrt{\frac{E_{\boldsymbol{p}\pm}-\xi_{\boldsymbol{p}\pm}}{E_{\boldsymbol{p}\pm}+\xi_{\boldsymbol{p}\pm}}}$.

From Eq. (21), one can find the singlet pairing amplitude,

$$\begin{aligned}\psi_{\uparrow\downarrow}(\boldsymbol{p}) &= \frac{\langle \mathrm{BCS}|\, c^\dagger_{\boldsymbol{p}\uparrow}c^\dagger_{-\boldsymbol{p}\downarrow}\,|\mathrm{BCS}\rangle}{\langle \mathrm{BCS}|\mathrm{BCS}\rangle} \\ &= -\frac{1}{2}\left(\frac{w_{\boldsymbol{p}+}}{1+w^2_{\boldsymbol{p}+}} + \frac{w_{\boldsymbol{p}-}}{1+w^2_{\boldsymbol{p}-}}\right) \\ &= -\frac{\Delta_0}{4}\sum_{\alpha=\pm} 1/E_{\vec{p},\alpha} \\ &= -\psi_{\downarrow\uparrow}(-\boldsymbol{p}) = -\psi_{\downarrow\uparrow}(\boldsymbol{p}),\end{aligned} \tag{22}$$

and the triplet pairing amplitude,

$$\begin{aligned}\psi_{\uparrow\uparrow}(\boldsymbol{p}) &= \frac{\langle \mathrm{BCS}|\, c^\dagger_{\boldsymbol{p}\uparrow}c^\dagger_{-\boldsymbol{p}\uparrow}\,|\mathrm{BCS}\rangle}{\langle \mathrm{BCS}|\mathrm{BCS}\rangle} \\ &= \frac{1}{2}\left(\frac{w_{\boldsymbol{p}+}}{1+w^2_{\boldsymbol{p}+}} - \frac{w_{\boldsymbol{p}-}}{1+w^2_{\boldsymbol{p}-}}\right)e^{i\varphi_{\boldsymbol{p}}} \\ &= -\frac{\Delta_0}{4}e^{i\varphi_{\vec{p}}}\sum_{\alpha=\pm}\alpha/E_{\vec{p},\alpha} \\ &= -\psi^*_{\downarrow\downarrow}(\boldsymbol{p}).\end{aligned} \tag{23}$$

Plugging into Eq. (9) leads to the many-body coherence length $\xi_i$ along different directions versus the SOC strength shown in Fig. 2. We also plot a reference line $k_F\xi_0 = 1$ ($k_F\xi_{0i} = \frac{1}{\sqrt{3}}$ for each component) to qualitatively signal the BCS to BEC crossover. As shown in Fig. 2, the coherence length in both the $x$ (or $y$) and $z$ directions decreases monotonically and sharply as the SOC strength increases for a fixed interaction strength $\frac{1}{k_Fa_s}$, and finally drops below the reference line. This is the most direct evidence that the Rashba SOC drives a crossover from BCS to BEC. The monotonic decreasing shape of the coherence length in Fig. 2 can be directly detected by a radio-frequency dissociation spectra experiment [38].

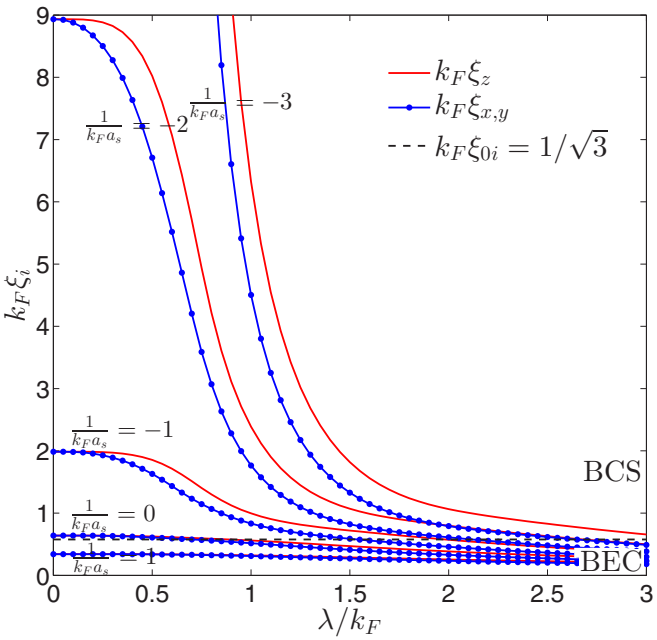


FIG. 2. (Color online) The coherence length defined in Eq. (9) along the $x$ direction (red lines) ($\xi_x = \xi_y$) and along the $z$ direction ( blue lines) as a function of 3D Rashba SOC strength $\lambda$. The dashed line is a guidance line where $k_F\xi_0 = 1$ ($k_F\xi_{0i} = 1/\sqrt{3}$ for each component). Starting from the BCS side at $\lambda = 0$, it decreases monotonically and quickly below the reference line, and so precisely describes the SOC-driven BCS to BEC crossover. Starting from the BEC side at $\lambda = 0$, the effects of SOC are small.

In the absence of the SOC when $\lambda = 0$, there is only a singlet pairing, and one can get an analytical result,

$$\begin{aligned}\xi^2_{x,y,z}(\lambda = 0) &= \frac{4\int dp p^{d+1}\frac{\xi^2_{\boldsymbol{p}}}{E^6_{\boldsymbol{p}}}}{d\,(2m)^2\int dp\frac{p^{d-1}}{E^2_{\boldsymbol{p}}}} \\ &= \frac{\sqrt{\frac{\eta(16\eta^4+52\eta^2+45)}{\eta^2+1}} + \frac{16\eta^4+44\eta^2+25}{\sqrt{\eta^2+1}}}{(2m\Delta)24\sqrt{\eta+\sqrt{\eta^2+1}}},\end{aligned} \tag{24}$$

where $\eta = \frac{\mu}{\Delta}$. In the weak-coupling (BCS) limit [37], $\frac{1}{k_Fa_s} \longrightarrow -\infty$, $\mu = E_F$, and $\Delta_0 = \frac{8E_F}{e^2}e^{\frac{\pi}{2k_Fa_s}} \longrightarrow 0$, $\xi_{x,y,z} = \frac{1}{\sqrt{6}}\frac{k_F}{2m\Delta_0} = \frac{1}{\sqrt{6}}\xi_{0\mathrm{BCS}}$, where $\xi_{0\mathrm{BCS}} = \frac{v_F}{2\Delta_0}$ is nothing but the coherence length [28] which goes to $\infty$ as $\frac{1}{k_Fa_s} \longrightarrow -\infty$. In the strong-coupling (BEC) limit [37], $\frac{1}{k_Fa_s} \longrightarrow \infty$, $\mu = -\frac{E_b}{2} + \frac{2k_Fa_s}{3\pi}E_F$, where $E_b = \frac{1}{ma_s^2}$ is the binding energy, and $\Delta_0 = \sqrt{\frac{16}{\pi k_Fa_s}}E_F$, so $\xi_{x,y,z} \to \frac{a_s}{\sqrt{6}}$, which recovers the two-body scattering length given by Eq. (31) [40].

The coherence lengths along different directions versus the scattering length are shown in Fig. 3 which is complementary to Fig. 2.

### C. Cooper-pair size across BCS to BEC crossover

As shown in Sec. II, the Cooper-pair size in Eq. (14) is another characteristic length in a Fermi-gas system. Formally,

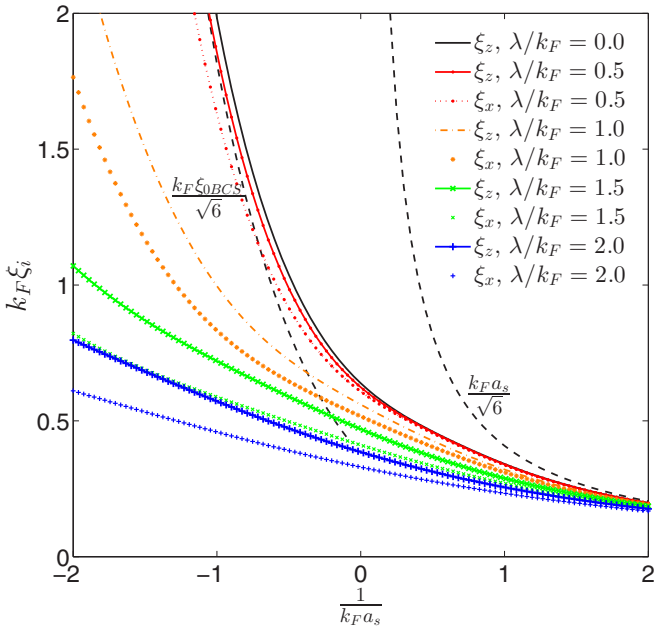


FIG. 3. (Color online) The coherence lengths $\xi_z > \xi_x = \xi_y$ at a fixed 3D Rashba SOC strength vs the scattering length. Different colors stand for different SOC strengths. The dark dashed line on the left is its BCS limit $\frac{1}{\sqrt{6}}k_F\xi_{0\mathrm{BCS}} = \frac{1}{8\sqrt{6}e^2}e^{-\frac{\pi}{2k_F a_s}}$ at $\lambda = 0$. On the right is its BEC limit $\frac{k_F a_s}{\sqrt{6}}$ at $\lambda = 0$. On the BCS side, the SOC effects are dramatic, but on the BEC side, the SOC effects are small, and all curves converge to the right dashed line $\frac{k_F a_s}{\sqrt{6}}$ from below.

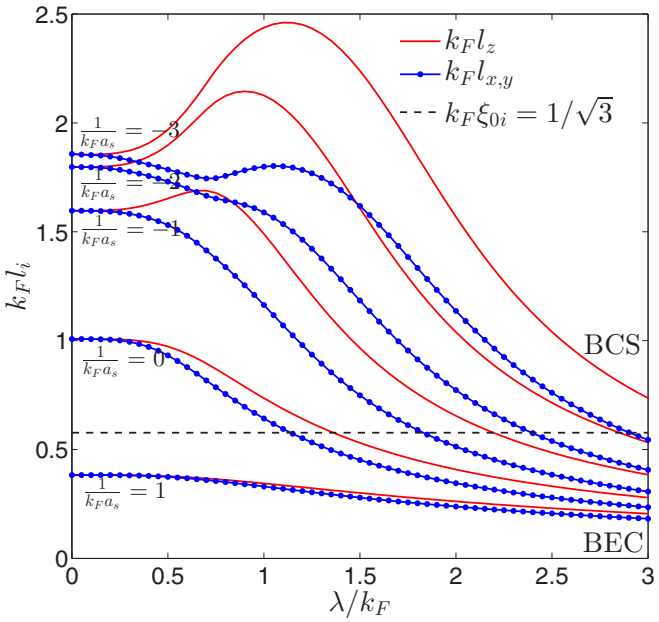


FIG. 4. (Color online) The Cooper-pair size defined in Eqs. (14) and (29) along the $x$ direction (red lines) ($l_x = l_y$) and $z$ direction (blue lines) as a function of 3D Rashba SOC strength $\lambda$. Note its nonmonotonic behaviors in the BCS side. The effects of SOC are small starting from the BEC side at $\lambda = 0$.

one can define the Cooper-pair wave function [15] in the second quantized form by removing the exponential in Eq. (21),

$$\begin{aligned}|g_{cp}\rangle &= \sum_{\boldsymbol{p}}{}' [w_{\boldsymbol{p}+} e^{-i\varphi_{\boldsymbol{p}}} h^\dagger_{\boldsymbol{p}+} h^\dagger_{-\boldsymbol{p}+} + w_{\boldsymbol{p}-} e^{i\varphi_{\boldsymbol{p}}} h^\dagger_{\boldsymbol{p}-} h^\dagger_{-\boldsymbol{p}-}]|0\rangle \\ &= \sum_{\boldsymbol{p}}{}' [g_{\uparrow\downarrow}(\boldsymbol{p}) c^\dagger_{\boldsymbol{p}\uparrow} c^\dagger_{-\boldsymbol{p}\downarrow} + g_{\downarrow\uparrow}(\boldsymbol{p}) c^\dagger_{\boldsymbol{p}\downarrow} c^\dagger_{-\boldsymbol{p}\uparrow} \\ &\quad + g_{\uparrow\uparrow}(\boldsymbol{p}) c^\dagger_{\boldsymbol{p}\uparrow} c^\dagger_{-\boldsymbol{p}\uparrow} + g_{\downarrow\downarrow}(\boldsymbol{p}) c^\dagger_{\boldsymbol{p}\downarrow} c^\dagger_{-\boldsymbol{p}\downarrow}]|0\rangle, \end{aligned} \tag{25}$$

which only has two paired fermions with both singlet and triplet pairing. In Eq. (25), we have used Eq. (17) and found

$$\begin{aligned} g_{\uparrow\downarrow}(\boldsymbol{p}) &= -\tfrac{1}{2}(w_{\boldsymbol{p}+} + w_{\boldsymbol{p}-}) = -g_{\downarrow\uparrow}(-\boldsymbol{p}) = -g_{\downarrow\uparrow}(\boldsymbol{p}), \\ g_{\uparrow\uparrow}(\boldsymbol{p}) &= \tfrac{1}{2}(w_{\boldsymbol{p}+} - w_{\boldsymbol{p}-}) e^{-i\varphi_{\boldsymbol{p}}} = -g^*_{\downarrow\downarrow}(\boldsymbol{p}). \end{aligned} \tag{26}$$

The corresponding first quantized form of Eq. (25) in real space is

$$\begin{aligned} g_{cp}(\vec{r}) &= g_{\uparrow\downarrow}(\vec{r})(|\uparrow\downarrow\rangle - |\downarrow\uparrow\rangle) \\ &\quad + g_{\uparrow\uparrow}(\vec{r})|\uparrow\uparrow\rangle - g^*_{\uparrow\uparrow}(\vec{r})|\downarrow\downarrow\rangle, \end{aligned} \tag{27}$$

where $g_{\alpha\beta}(\vec{r}) = \sum_{\vec{p}} e^{i\vec{p}\cdot\vec{r}} g_{\alpha\beta}(\vec{p})$, $\alpha,\beta = \uparrow,\downarrow$. Compared to Eq. (11), one can see that there are two extra equal-spin $p_x \pm ip_y$ pairing components [29] similar to the $A$ phase of $^3$He.

It is easy to see that the Cooper-pair size along the $i$ direction in Eq. (14) can be expressed as

$$l_i^2 = \frac{\langle g_{cp}|r_i^2|g_{cp}\rangle}{\langle g_{cp}|g_{cp}\rangle}, \quad i = x,y,z, \tag{28}$$

which has a clear physical meaning: the Cooper-pair size is the "average size" of the Cooper-pair wave function given by Eq. (27). Shown in Fig. 4 is the Cooper-pair size along different directions versus the SOC strength. In sharp contrast to the coherence length, it is nonmonotonic [41] in the BCS side $a_s < 0$, so it may not be a good quantity to characterize the BCS to BEC crossover. Furthermore, it may not be an experimentally detectable quantity anyway.

In the absence of the SOC when $\lambda = 0$, there is only a singlet pairing, and Eq. (28) is simplified to

$$l_i^2(\lambda = 0) = \frac{\sum_{\boldsymbol{k}} \left(1 - \frac{\xi_{\boldsymbol{k}}}{E_{\boldsymbol{k}}}\right)^2 \frac{k^2}{m^2}}{3\sum_{\boldsymbol{k}}(E_{\boldsymbol{k}} - \xi_{\boldsymbol{k}})^2}. \tag{29}$$

In the weak-coupling (BCS) limit (i.e., $\frac{1}{k_F a_s} \longrightarrow -\infty$), $\mu = E_F$, and $\Delta \to 0$, one finds $l_{x,y,z} \longrightarrow \sqrt{\frac{7}{2}}\frac{1}{k_F}$, which is nothing but the interparticle distance, in sharp contrast to the coherence length, which is nothing but the coherence length. Using $l_{0\mathrm{BCS}} \sim \frac{k_F}{2m\epsilon_F}$, $\xi_{0\mathrm{BCS}} \sim \frac{k_F}{2m\Delta_0}$, one can see their ratio, $l_{0\mathrm{BCS}}/\xi_{0\mathrm{BCS}} \sim \Delta_0/\epsilon_F = \frac{8}{e^2}e^{\frac{\pi}{2k_F a_s}} \longrightarrow 0$. For conventional superconductors, $l_{0\mathrm{BCS}}/\xi_{0\mathrm{BCS}} \sim 10^{-4}$, which indicates that there are about $10^4$ other Cooper pairs inside a given Cooper pair. However, for high-$T_c$ superconductors [29,31], $l_{0\mathrm{BCS}}/\xi_{0\mathrm{BCS}} \sim 10^{-1}$, which indicates that they are quite close to the BCS to BEC crossover, but still in the BCS side.

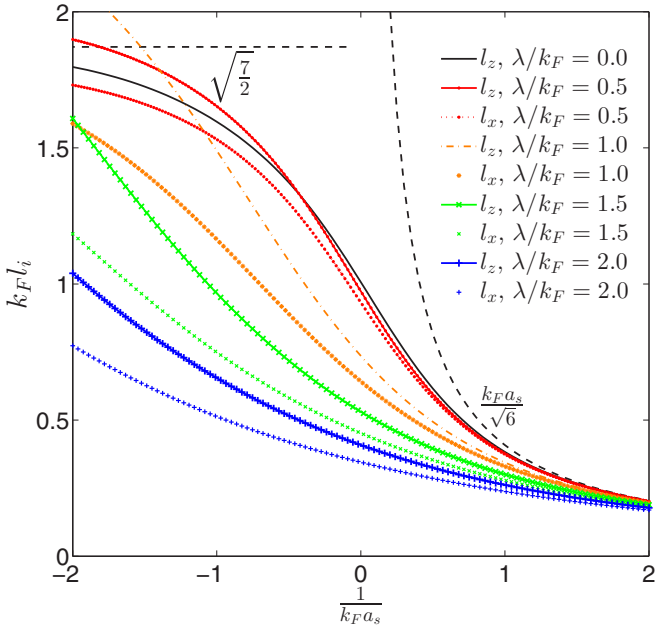


FIG. 5. (Color online) The Cooper-pair size $l_z > l_x = l_y$ at a fixed 3D Rashba SOC vs the scattering length. Different colors stand for different SOC strengths. The dark dashed line on the left is its BCS limit $\sqrt{7/2}$ at $\lambda = 0$. On the right is its BEC limit $\frac{k_F a_s}{\sqrt{6}}$ at $\lambda = 0$. On the BCS side, the SOC effects are dramatic, but on the BEC side, the SOC effects are small, and all curves converge to the right dashed line $\frac{k_F a_s}{\sqrt{6}}$ from below.

In the BEC limit, we find $l_i \to \frac{a_s}{\sqrt{6}}$, which also recovers the two-body scattering length given by Eq. (31) [40]. So, $l_{0\mathrm{BCS}}/\xi_{0\mathrm{BCS}} = 1$ in the strong BEC limit. This should be expected because the Cooper-pair wave function is nothing but the two-fermion component of the many-body wave function, so both lengths have to be the same in the strong BEC limit.

The Cooper-pair sizes along different directions versus the scattering length is shown in Fig. 5, which is complementary to Fig. 4.

### D. Contrast with two-body wave functions

The two-body wave function with a 3D Rashba SOC was worked out in [14] by solving a two-body Schrödinger equation [28]. It is instructive to compare the many-body wave functions given by Eq. (21) and the Cooper-pair wave function given by Eq. (26) with the corresponding two-body wave functions (see the extreme oblate case in [14]). They all have the same symmetries, namely,

$$\begin{aligned} \psi_{\uparrow\downarrow}(\boldsymbol{p}) &= -\psi_{\downarrow\uparrow}(\boldsymbol{p}), \quad g_{\uparrow\downarrow}(\boldsymbol{p}) = -g_{\downarrow\uparrow}(\boldsymbol{p}), \\ \psi_{\uparrow\uparrow}(\boldsymbol{p}) &= -\psi^*_{\downarrow\downarrow}(\boldsymbol{p}), \quad g_{\uparrow\uparrow}(\boldsymbol{p}) = -g^*_{\downarrow\downarrow}(\boldsymbol{p}). \end{aligned} \tag{30}$$

However, they have quite different behaviors. It was shown that in the absence of the SOC when $\lambda = 0$, there exists a bound state in the BEC side only with $a_s > 0$, and the bound state has only a singlet component $\psi_0(\vec{r}) = \frac{1}{r} e^{-r/a_s}$ with a binding energy $E_b = \frac{1}{m a_s^2}$. It is easy to see the size of the bound state:

$$b(\lambda = 0) = \sqrt{\frac{\langle\psi_0|r^2|\psi_0\rangle}{\langle\psi_0|\psi_0\rangle}} = \frac{a_s}{\sqrt{2}}, \tag{31}$$

which is identical to both the coherence length given by Eq. (9) and the Cooper-pair size given by Eq. (14) in the BEC limit [40]. As shown in Fig. 1, in the absence of the SOC when $\lambda = 0$, the coherence length $\xi_i$ and Cooper-pair size $l_i$ are well defined in both the BCS and BEC limit.

However, as shown in [14], a nonzero SOC strength $\lambda \neq 0$ will always lead to a two-body bound state at any $a_s$, and extending the $b(\lambda = 0)$ in Eq. (31) to a nonzero $\lambda$ can be easily calculated using the two-body wave functions in [14,20]. Any nonzero SOC strength, as shown in Fig. 1, leads to $\xi_z > \xi_x = \xi_y$ and $l_z > l_x = l_y$. In the BCS side, $\xi_i$ and $l_i$ display dramatically different behaviors, while in the BEC limit, both $\xi_i$ and $l_i$ converge to the size of the two-body bound state. This is expected because in the strong BEC limit the overlap between the two-body wave function and the many-body wave function must be the same as that between the two-body wave function and the Cooper-pair wave function.

## IV. 3D FERMI GAS WITH AN ISOTROPIC WEYL SOC

The 3D Weyl SOC term $V_{\mathrm{Weyl}} = \lambda \vec{k} \cdot \vec{\sigma}$ can be written in the second quantization form,

$$\begin{aligned} V_{\mathrm{Weyl}} = \frac{\lambda}{m} \sum_{\boldsymbol{p}} [ & p_\perp (e^{-i\varphi_{\boldsymbol{p}}} c^\dagger_{\boldsymbol{p}\uparrow} c_{\boldsymbol{p}\downarrow} + e^{i\varphi_{\boldsymbol{p}}} c^\dagger_{\boldsymbol{p}\downarrow} c_{\boldsymbol{p}\uparrow}) \\ & + p_z (c^\dagger_{\boldsymbol{p}\uparrow} c_{\boldsymbol{p}\uparrow} - c^\dagger_{\boldsymbol{p}\downarrow} c_{\boldsymbol{p}\downarrow})]. \end{aligned} \tag{32}$$

The single-particle part in the Hamiltonian given by Eq. (1) can be diagonalized in the helicity bases as $H_0 = \sum_{\boldsymbol{p}} (\xi_{\boldsymbol{p}+} h^\dagger_{\boldsymbol{p}+} h_{\boldsymbol{p}+} + \xi_{\boldsymbol{p}-} h^\dagger_{\boldsymbol{p}-} h_{\boldsymbol{p}-})$, where $\xi_{\boldsymbol{p}\pm} = \frac{p^2}{2m} \pm \frac{\lambda p}{m} - \mu$ and the helicity operators

$$\begin{aligned} h_{\boldsymbol{p}+} &= \sqrt{\frac{1}{2}} \left[ \sqrt{\frac{p + p_z}{p}} c_{\boldsymbol{p}\uparrow} + \sqrt{\frac{p - p_z}{p}} e^{-i\varphi_{\boldsymbol{p}}} c_{\boldsymbol{p}\downarrow} \right], \\ h_{\boldsymbol{p}-} &= \sqrt{\frac{1}{2}} \left[ \sqrt{\frac{p - p_z}{p}} e^{i\varphi_{\boldsymbol{p}}} c_{\boldsymbol{p}\uparrow} - \sqrt{\frac{p + p_z}{p}} c_{\boldsymbol{p}\downarrow} \right]. \end{aligned} \tag{33}$$

In the mean-field theory, the total Hamiltonian can also be diagonalized as Eq. (18), and the quasiparticle excitation energy $E_{\boldsymbol{p}\pm} = \sqrt{\xi^2_{\boldsymbol{p}\pm} + |\Delta_0|^2}$; the Bogoliubov quasiparticle operators take the same form as Eq. (19). At zero temperature, the two self-consistent equations also take the same form as Eq. (20), with the corresponding $\xi_{\boldsymbol{p}\pm}$ and $E_{\boldsymbol{p}\pm}$ defined above. Solving them leads to the chemical potential shown in Fig. 6. Similar to Fig. 1, the Weyl SOC also drives a new crossover from BCS to BEC.

### A. Coherence length

The wave function stays the same as Eq. (21), with the corresponding $\xi_{\boldsymbol{p}\pm}$ and $E_{\boldsymbol{p}\pm}$ defined above. Similar to

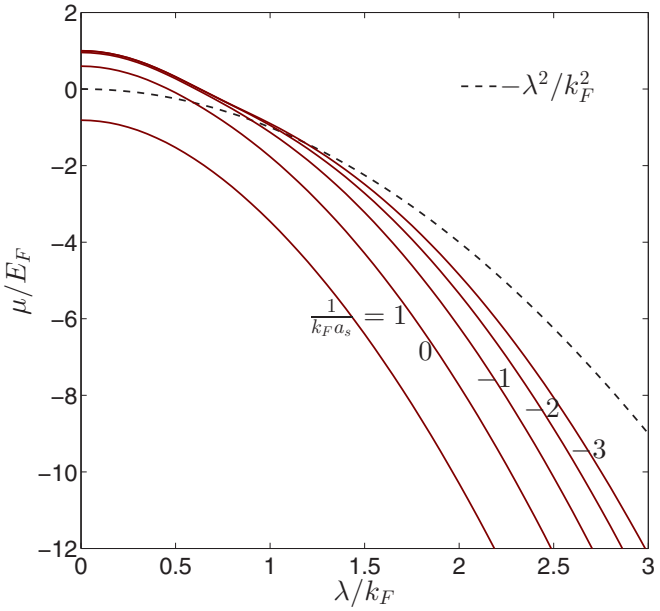


FIG. 6. (Color online) The chemical potential $\mu$ vs the 3D isotropic Weyl SOC strength $\lambda$ for different scattering lengths. The black dashed line $\mu_0 = -\frac{\lambda^2}{2m}$ is the chemical potential at the bottom of the single-particle spectrum. Starting from the BCS side at $\lambda = 0$, as $\lambda$ increases, the $\mu$ drops below $\mu_0$, indicating a crossover from BCS to BEC.

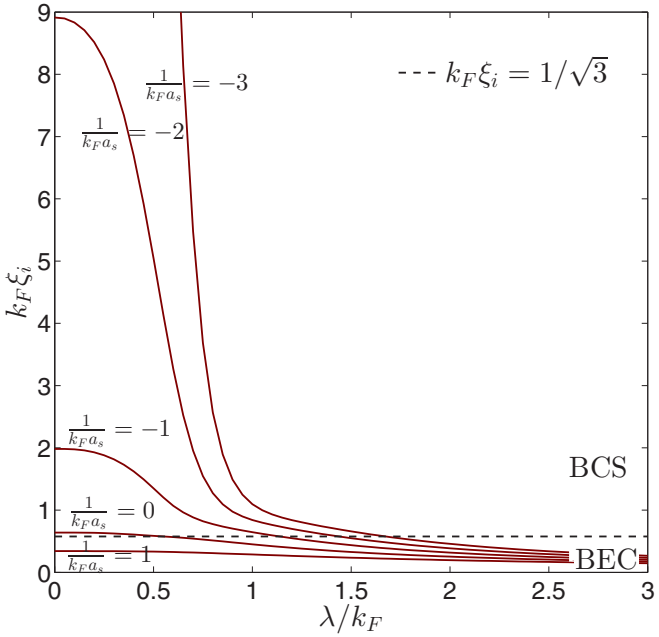


FIG. 7. (Color online) From the BCS side at $\lambda = 0$, the coherence length $\xi_x = \xi_y = \xi_z$ of 3D Weyl SOC decreases quickly and monotonically as the $\lambda$ increases and drops below the dashed line. It precisely describes the SOC-driven BCS to BEC crossover. The dashed line is a contrasting line where $k_F\xi_0 = 1$ (for each component, $k_F\xi_{0i} = 1/\sqrt{3}$). From the BEC side at $\lambda = 0$, the effects of SOC are small.

Sec. III B, we can determine the singlet pairing amplitude,

$$\psi_{\substack{\uparrow\downarrow\\ \downarrow\uparrow}}(\boldsymbol{p}) = \frac{\langle \mathrm{BCS}|\, c^\dagger_{\boldsymbol{p}\uparrow} c^\dagger_{-\boldsymbol{p}\downarrow}\, |\mathrm{BCS}\rangle}{\langle \mathrm{BCS}|\mathrm{BCS}\rangle} = \mp\frac{1}{2}\left(\frac{w_{\boldsymbol{p}+}}{1+w^2_{\boldsymbol{p}+}} + \frac{w_{\boldsymbol{p}-}}{1+w^2_{\boldsymbol{p}-}}\right) - \frac{1}{2}\left(\frac{w_{\boldsymbol{p}+}}{1+w^2_{\boldsymbol{p}+}} - \frac{w_{\boldsymbol{p}-}}{1+w^2_{\boldsymbol{p}-}}\right)\frac{p_z}{p},$$

and triplet pairing amplitude

$$\psi_{\uparrow\uparrow}(\boldsymbol{p}) = \frac{\langle \mathrm{BCS}|\, c^\dagger_{\boldsymbol{p}\uparrow} c^\dagger_{-\boldsymbol{p}\uparrow}\, |\mathrm{BCS}\rangle}{\langle \mathrm{BCS}|\mathrm{BCS}\rangle} = \frac{1}{2}\left(\frac{w_{\boldsymbol{p}+}}{1+w^2_{\boldsymbol{p}+}} - \frac{w_{\boldsymbol{p}-}}{1+w^2_{\boldsymbol{p}-}}\right)\frac{p_\perp}{p}e^{i\varphi_p} = -\psi^*_{\downarrow\downarrow}(\boldsymbol{p}),$$

where $w_{\boldsymbol{p}\pm} = \sqrt{\frac{E_{\boldsymbol{p}\pm}-\xi_{\boldsymbol{p}\pm}}{E_{\boldsymbol{p}\pm}+\xi_{\boldsymbol{p}\pm}}}$.

The coherence length $\xi_i$ can be calculated using Eq. (9) and is shown in Fig. 7. As the Weyl SOC strength increases, in the BCS side, the coherence length along any direction decreases monotonically and quickly, then drops below the dashed line. In the BEC side, the effects of the SOC strength are quite small. This is the most direct evidence that the Weyl SOC can also drive a crossover from BCS to BEC and can be directly detected by the type of experiment presented in Ref. [38].

The coherence lengths versus the scattering length are shown in Fig. 8, which is complementary to Fig. 7.

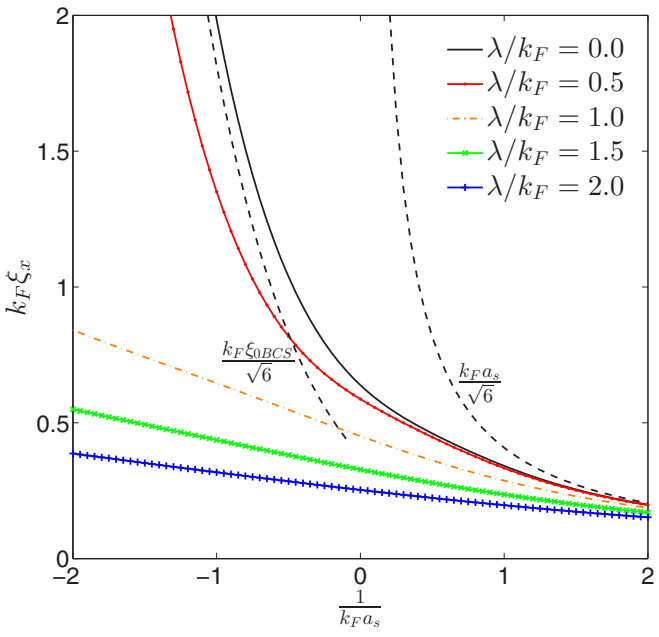


FIG. 8. (Color online) The coherence lengths $\xi_i$ of 3D Weyl SOC at a fixed SOC vs the scattering length. Different colored lines stand for different SOC strengths. The dark dashed line on the left is its BCS limit $\frac{1}{\sqrt{6}}k_F\xi_{0\mathrm{BCS}} = \frac{1}{8\sqrt{6e^2}}e^{-\frac{\pi}{2k_F a_s}}$ at $\lambda = 0$. On the left is its BEC limit $\frac{k_F a_s}{\sqrt{6}}$ at $\lambda = 0$. On the BCS side, the SOC effects are dramatic, but on the BEC side, the SOC effects are small, and all curves converge to the right dashed line $\frac{k_F a_s}{\sqrt{6}}$ from below. Compare with Fig. 3.

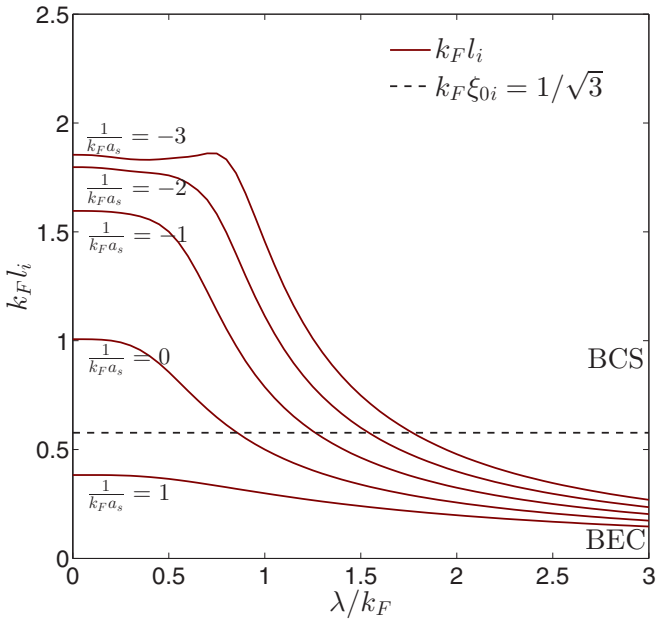


FIG. 9. (Color online) The Cooper-pair size $l_x = l_y = l_z$ of 3D Weyl SOC as a function of $\lambda$. Note its nonmonotonic behavior at the BCS side. The SOC effects on the BEC side are small.

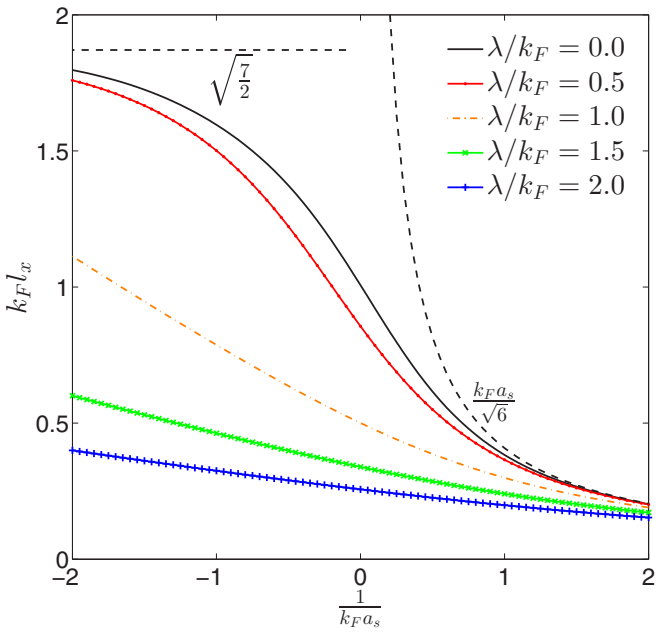


FIG. 10. (Color online) The Cooper-pair size $l_i$ of 3D Weyl SOC at a fixed SOC vs the scattering length. Different colored lines stand for different SOC strengths. The dark dashed line on the left is its BCS limit $\sqrt{7/2}$ at $\lambda = 0$. On the right is its BEC limit $\frac{k_F a_s}{\sqrt{6}}$ at $\lambda = 0$. On the BCS side, the SOC effects are dramatic, but on the BEC side, the SOC effects are small, and all curves converge to the right dashed line $\frac{k_F a_s}{\sqrt{6}}$ from below. Compare with Fig. 5.

### B. Cooper-pair size

The Cooper-pair wave function takes the same form as Eq. (25) in the second quantized form and Eq. (27) in the first quantized form with the corresponding $\xi_{p\pm}$ and $E_{p\pm}$ defined above. All the components can be written as

$$\begin{aligned} g_{\uparrow\downarrow}(\boldsymbol{p}) &= -\frac{1}{2}(w_{p+} + w_{p-}) - \frac{1}{2}(w_{p+} - w_{p-})\frac{p_z}{p} \\ &= -g_{\downarrow\uparrow}(-\boldsymbol{p}), \\ g_{\downarrow\uparrow}(\boldsymbol{p}) &= \frac{1}{2}(w_{p+} + w_{p-}) - \frac{1}{2}(w_{p+} - w_{p-})\frac{p_z}{p}, \\ g_{\uparrow\uparrow}(\boldsymbol{p}) &= \frac{1}{2}(w_{p+} - w_{p-})\frac{p_\perp}{p}e^{-i\varphi_p} = -g^*_{\downarrow\downarrow}(\boldsymbol{p}). \end{aligned} \tag{34}$$

The Cooper-pair size can be evaluated using Eq. (28) and plotted in Fig. 9. Its nonmonotonic behaviors at the BCS side indicate it may not be a good quantity to characterize the crossover.

The Cooper-pair sizes versus the scattering length are shown in Fig. 10, which is complementary to Fig. 9.

### C. Contrast with the two-body wave functions

To explore the relations between the many-body wave functions or the Cooper-pair wave function studied in this section and the two-body wave functions in [14], it is convenient to introduce the spin eigenstate along the momentum $\frac{\boldsymbol{p}}{p} = (\sin\theta\cos\varphi, \sin\theta\sin\varphi, \cos\theta)$,

$$\begin{aligned} |\uparrow\rangle_{\boldsymbol{p}} &= e^{-i\frac{\varphi}{2}}\cos\frac{\theta}{2}|\uparrow\rangle + e^{i\frac{\varphi}{2}}\sin\frac{\theta}{2}|\downarrow\rangle, \\ |\downarrow\rangle_{\boldsymbol{p}} &= e^{-i\frac{\varphi}{2}}\sin\frac{\theta}{2}|\uparrow\rangle - e^{i\frac{\varphi}{2}}\cos\frac{\theta}{2}|\downarrow\rangle, \end{aligned}$$

then express the many-body wave functions in terms of the spin eigenstates along the momentum $\vec{p}$,

$$\begin{aligned} & g_{\uparrow\downarrow}(\boldsymbol{p})|\uparrow\downarrow\rangle + g_{\downarrow\uparrow}(\boldsymbol{p})|\downarrow\uparrow\rangle + g_{\uparrow\uparrow}(\boldsymbol{p})|\uparrow\uparrow\rangle + g_{\downarrow\downarrow}(\boldsymbol{p})|\downarrow\downarrow\rangle \\ &= -\frac{1}{2}(w_{p+} + w_{p-})(|\uparrow\downarrow\rangle - |\downarrow\uparrow\rangle) + \frac{1}{2}(w_{p+} - w_{p-}) \\ &\quad \times\left[\frac{p_x - ip_y}{p}|\uparrow\uparrow\rangle - \frac{p_z}{p}(|\uparrow\downarrow\rangle + |\downarrow\uparrow\rangle)\right. \\ &\quad \left. - \frac{p_x + ip_y}{p}|\downarrow\downarrow\rangle\right] \\ &= -\frac{1}{2}(w_{p+} + w_{p-})(|\uparrow\downarrow\rangle - |\downarrow\uparrow\rangle) \\ &\quad + \frac{1}{2}(w_{p+} - w_{p-})(|\uparrow\downarrow\rangle_{\boldsymbol{p}} + |\downarrow\uparrow\rangle_{\boldsymbol{p}}) \\ &\equiv g_a(p)(|\uparrow\downarrow\rangle - |\downarrow\uparrow\rangle) + g_s(p)(|\uparrow\downarrow\rangle_{\boldsymbol{p}} + |\downarrow\uparrow\rangle_{\boldsymbol{p}}), \end{aligned} \tag{35}$$

where the components $g_a(p)$ and $g_s(p)$ are independent of the direction of $\boldsymbol{p}$ (i.e., $\theta$ and $\varphi$). Compared to Eq. (11), one can see that there are three extra $p_x \pm ip_y$ and $p_z$ pairing components [29] similar to the $B$ phase of superfluid $^3$He. This fact should be contrasted to Eq. (27) where there are only two extra equal-spin $p_x \pm ip_y$ pairing components [29], similar to the $A$ phase of superfluid $^3$He.

Fourier transforming the Cooper-pair wave function given by Eq. (35) to real space and comparing with the two-body wave function in the spherical case in [14], we find that they have the same symmetry. In fact, a similar relation between the wave functions (or order parameters) in real space and those

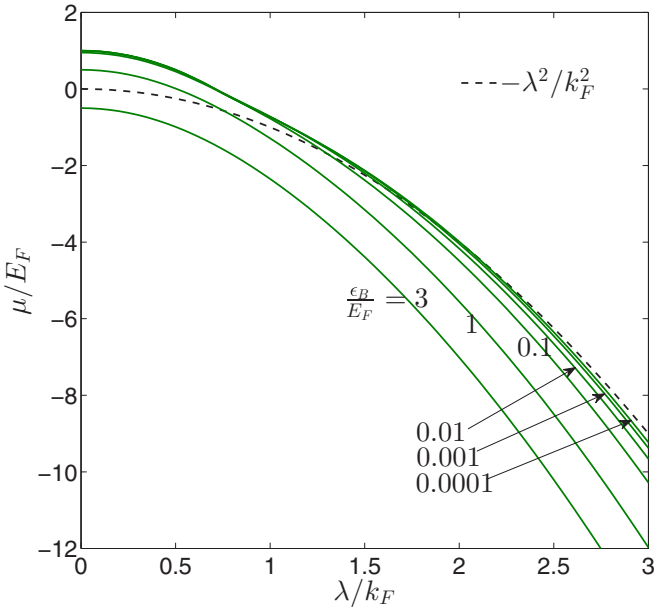


FIG. 11. (Color online) The chemical potential $\mu$ vs $\lambda$ in a 2D isotropic SOC system for different scattering lengths. The dashed line is the minimum energy of the single particle $\mu_0 = -\frac{\lambda^2}{2m}$. On the BCS side, as $\lambda$ increases, the $\mu$ drops below $\mu_0$, indicating a crossover from a BCS to BEC crossover.

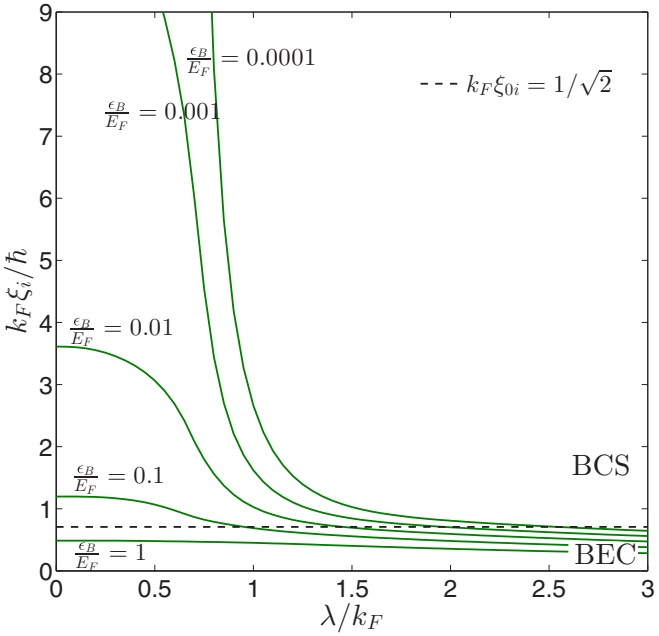


FIG. 12. (Color online) The 2D coherence length defined in Eq. (9) ($\xi_x = \xi_y$) as a function of $\lambda$. At the BCS side, it decreases quickly and monotonically as the $\lambda$ increases and drops below the dashed line. It precisely describes the SOC-driven BCS to BEC crossover. The dashed line is a guidance line, where $k_F\xi_0 = 1$ (on average, $k_F\xi_{0i} = 1/\sqrt{2}$). At the BEC side, the effects of SOC are small.

in the helicity momentum basis were derived for magnetic transitions in repulsively interacting Fermi gas [23].

## V. 2D FERMI GAS WITH A RASHBA SOC

A 2D Rashba SOC term $V_{2D-ra} = -i\lambda(\partial_x\sigma_x + \partial_y\sigma_y)$ can be written in the second quantization form,

$$V_{2D-ra} = \frac{\lambda}{m}\sum_{\boldsymbol{p}} p[e^{-i\varphi_{\boldsymbol{p}}}c^\dagger_{\boldsymbol{p}\uparrow}c_{\boldsymbol{p}\downarrow} + e^{i\varphi_{\boldsymbol{p}}}c^\dagger_{\boldsymbol{p}\downarrow}c_{\boldsymbol{p}\uparrow}], \qquad (36)$$

where $\lambda$ is the strength of the SOC, $p = \sqrt{p_x^2 + p_y^2}$, and $\varphi_{\boldsymbol{p}} = \mathrm{Arg}(p_x + ip_y)$. Note that the space is 2D, but the spin is still SU(2) with the three generators.

The BCS theory in two dimensions has been studied in several works [42,43] with a different focus. The calculations are similar to the 3D Rashba case in Sec. III with the momentum $\vec{p}$ confined to be the 2D momentum $\vec{p}_\perp$, or similar to the 3D Weyl case in Sec. IV by setting $p_z = 0$. Equations (16)–(19) follow. The two self-consistent equations (20) also hold, with the crucial difference that the interaction needs to be regularized by a bound-state energy $\epsilon_B$ at 2D, instead of a scattering length $a_s$ in 3D: $\frac{1}{g} = -\frac{1}{V}\sum_{\boldsymbol{p}}\frac{1}{2\epsilon_{\boldsymbol{p}}+\epsilon_B}$. Solving them leads to the chemical potential $\mu$ shown in Fig. 11.

### A. Coherence length

When calculating the coherence length, Eqs. (21)–(23) still hold. For $\lambda \neq 0$, only numerical results are available and are shown in Fig. 12. We can see that in the BCS limit at $\lambda = 0$, as the strength of SOC increases for a fixed interaction strength $\frac{\epsilon_B}{E_F}$, the pair size decreases monotonically and sharply, then goes below the reference line. Here, we also plot a reference

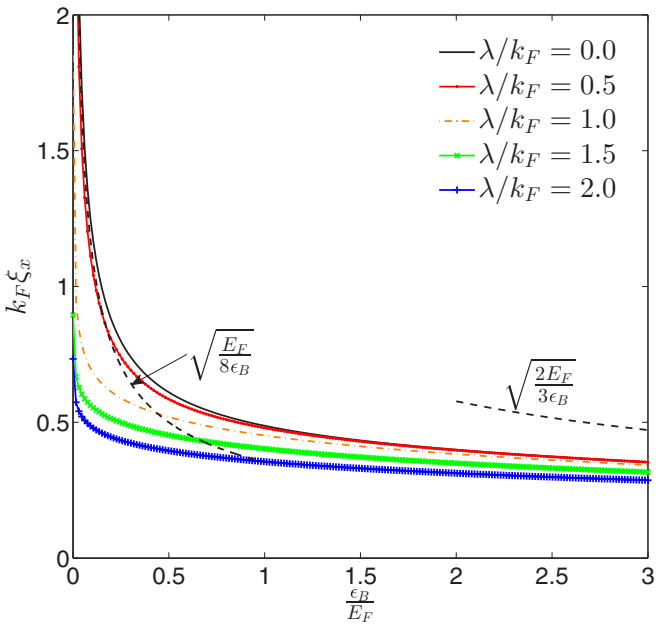


FIG. 13. (Color online) The 2D coherence lengths $\xi_x = \xi_y$ at a fixed SOC vs the scattering length. Different colored lines stand for different SOC strengths. The black dashed line on the left is its BCS limit $\sqrt{\frac{E_F}{8\epsilon_B}}$ at $\lambda = 0$. On the right is its BEC limit $\sqrt{\frac{2E_F}{3\epsilon_B}}$ at $\lambda = 0$. On the BCS side, the SOC effects are dramatic, but on the BEC side, the SOC effects are small, and all curves converge to the right dashed line $\sqrt{\frac{2E_F}{3\epsilon_B}}$ from below.

line by taking $k_F\xi_0 = 1$ (for each component, $k_F\xi_{0i} = \frac{1}{\sqrt{2}}$) to qualitatively observe the BCS to BEC crossover behavior. In the BEC limit, the effects of SOC are small.

Setting $\lambda = 0$, one can easily solve the self-consistent equations and find $\mu = E_F - \frac{|\epsilon_B|}{2}$ and $\Delta = \sqrt{2|\epsilon_B|E_F}$. When $\lambda = 0$, Eq. (24) at $d = 3$ should be replaced by [42,43]

$$\xi_{x,y}^2(\lambda = 0) = \frac{4\int dp p^{d+1}\frac{\xi_p^2}{E_p^6}}{(2m)^2 d\int dp\frac{p^{d-1}}{E_p^2}} = \frac{1}{4(2m\Delta)}\left(\eta + \frac{\eta^2+2}{\eta^2+1}\frac{1}{\frac{\pi}{2}+\arctan\eta}\right), \quad (37)$$

where $\eta = \frac{\mu}{\Delta}$. Because of different dimensions, this analytical expression is very different from Eq. (24) in 3D. In the BCS limit (i.e., $\frac{\epsilon_B}{E_F} \longrightarrow 0$), $\eta = \frac{1}{\sqrt{2}}\sqrt{\frac{E_F}{|\epsilon_B|}} \longrightarrow \infty$, $k_F\xi_{x,y} \longrightarrow \sqrt{\frac{E_F}{8|\epsilon_B|}}$, which diverges. In the BEC limit (i.e., $\frac{|\epsilon_B|}{E_F} \longrightarrow \infty$), $\mu = -\frac{|\epsilon_B|}{2}$ and $\eta = -\frac{1}{2\sqrt{2}}\sqrt{\frac{|\epsilon_B|}{E_F}} \longrightarrow -\infty$, $k_F\xi_{x,y} \to \sqrt{\frac{3}{2}\frac{E_F}{|\epsilon_B|}}$.

Shown in Fig. 13 is the coherence length versus the scattering length, which is complementary to Fig. 12.

### B. Cooper-pair size

When calculating the Cooper-pair size, Eqs. (25)–(28) still hold. Shown in Fig. 14 is how the Cooper-pair size changes with $\lambda$. Once more, its nonmonotonic behaviors at the BCS side indicate it may not be a good quantity to characterize the BCS to BEC crossover.

When $\lambda = 0$, Eq. (29) at $d = 3$ should be replaced by

$$l_i^2(\lambda = 0) = \frac{3\left[\ln 2 - \frac{1}{2} - \eta\left(\frac{\pi}{2} + \arctan\eta\right) - \ln\left(1 - \frac{\eta}{\sqrt{\eta^2+1}}\right) + \eta(\eta + \sqrt{\eta^2+1})\right]}{2m\Delta\left[\eta^3 + (\eta^2+1)^{\frac{3}{2}} + \frac{3}{2}\eta\right]}, \quad (38)$$

where $\eta = \frac{\mu}{\Delta}$. In the BCS limit (i.e., $\frac{\epsilon_B}{E_F} \longrightarrow 0$), one get $l_{x,y} \longrightarrow \sqrt{3}\frac{1}{k_F}$, which is nothing but the interparticle distance, so it goes to a finite value, in sharp contrast to the coherence length, which diverges. In fact, $l/\xi \sim \Delta_0/\epsilon_F \to 0$ in the BCS limit. In the BEC limit (i.e., $\frac{|\epsilon_B|}{E_F} \longrightarrow \infty$), one find $k_F l_{x,y} = \sqrt{\frac{2E_F}{3|\epsilon_B|}}$, which is identical to $k_F\xi_{x,y}$ in the BEC limit, as it should be.

Shown in Fig. 15 is the Cooper-pair size at various fixed SOC strengths versus the bound-state energies $\epsilon_B/E_F$, which is complementary to Fig. 14.

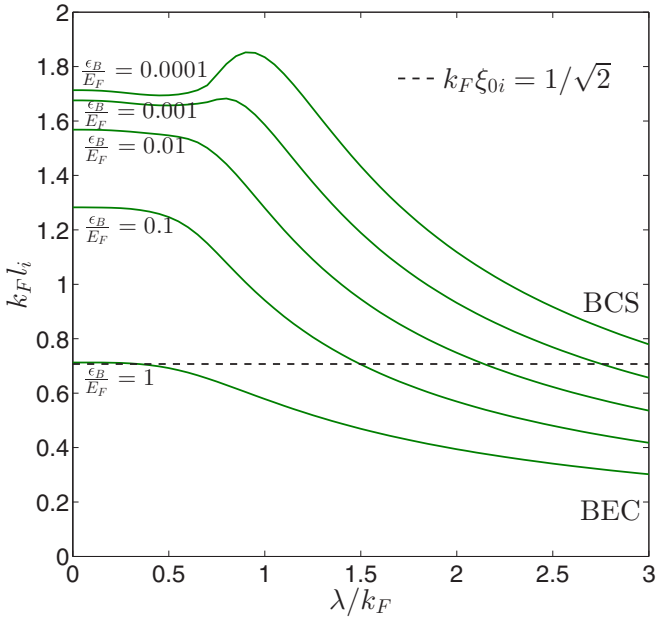


FIG. 14. (Color online) The 2D Cooper-pair size $l_x = l_y$ as a function of $\lambda$. Note its nonmonotonic behavior at the BCS side.

## VI. APPLICATIONS TO 2D SUPERCONDUCTOR AND SEMICONDUCTOR SYSTEMS

In various 3D condensed-matter systems [1,7], the 3D SOCs usually take $\lambda(\vec{k}\times\vec{\sigma})\cdot\nabla V$, which is a quite different form from the Weyl or Rashba forms studied in Secs. III and IV by keeping the inversion symmetry. It may be interesting to see if

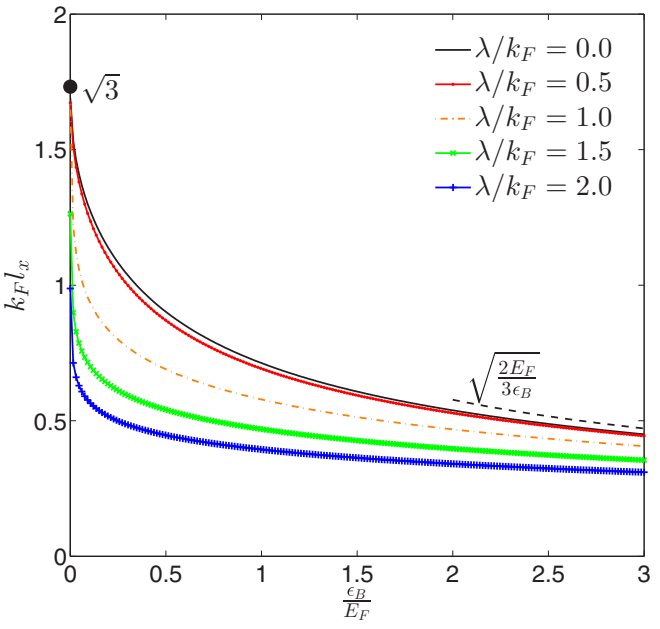


FIG. 15. (Color online) The 2D Cooper-pair size $l_x = l_y$ at a fixed SOC vs the scattering length. Different colored lines stand for different SOC strengths. The black dot on the left is its BCS limit $\sqrt{3}$ at $\lambda = 0$. On the right is its BEC limit $\sqrt{\frac{2E_F}{3\epsilon_B}}$ at $\lambda = 0$. On the BCS side, the SOC effects are dramatic, but on the BEC side, the SOC effects are small, and all curves converge to the right dashed line $\sqrt{\frac{2E_F}{3\epsilon_B}}$ from below.

such a 3D inversion symmetric SOC can also drive a BCS to BEC crossover.

Equation (1) with the 2D Rashba SOC term given by Eq. (36) may also describe a 2D bright exciton with total angular momentum $J = \pm 1$ in electron-hole semiconductor bilayer systems and electron pairings in 2D noncentrosymmetric superconductors [2–4]. It was known that in a 2D semiconductor electron gas, the 2D Rashiba SOC strength depends on the electric field, the presence of adatoms at the boundary, atomic weight, and atomic shells involved [2,5,6]. In the surface of noncentrosymmetric superconductors, the strong near-surface electric fields lead to a 2D Rashba SOC quite similar to the 2D superconducting fullerene and polyacene crystals in the field-effect-transistor geometry [2]. So the 2D Rashba SOC strength in the two condensed-matter systems can also be tuned by adjusting various surface geometries. Therefore, the results achieved on the BCS to BEC crossover tuned by the 2D Rashba strength in Sec. V should also apply to these condensed-matter systems. In Refs. [32–35], the authors ignored the spins of the fermions and holes, therefore also the possible Rashba SOC. As shown at the end of [34], the bright excitons couple to the one-photon process with the polarization $\sigma = \pm$. By incorporating the coupling between the 2D bright excitons subject to the 2D Rashba SOC studied in Sec. V and the 3D emitted photons with the two polarizations, it is interesting to study how the emitted photon characteristics change across the SOC-driven BCS to BEC crossover.

## VII. DISCUSSIONS AND CONCLUSIONS

The new BCS to BEC crossover driven by the SOC strength has been studied by previous authors from the overlap between a Cooper-pair wave function and two-body wave function [15], and also from the Cooper-pair size right at the Feshbach resonance [16]. In this paper, we investigate the SOC-driven BCS to BEC crossover from fundamental and physical points of view. At the mean-field level, we studied the dependence of chemical potential, coherence length, and Cooper-pair size on the SOC strength for three kinds of Fermi gases with 3D Rashba, 3D Weyl, and 2D Rashba SOC, respectively. We explicitly demonstrated the SOC-driven BCS to BEC crossover in all three cases by monitoring the monotonic decreasing of chemical potential and the coherence length. We show that the most relevant wave function is the many-body wave function instead of the Cooper-pair wave function or two-body wave function; the most relevant length is the coherence length instead of the Cooper-pair size or the two-body bound-state size. Among the three lengths, only the coherence length is the experimentally detectable length.

We can summarize the main differences among the coherence length, the Cooper-pair size, and the two-body size in the following: In the absence of SOC, in the BCS limit, the coherence length goes to the coherence length $\xi(\lambda = 0) = v_F/\Delta_0$, while the Cooper-pair size goes to the interparticle distance $l(\lambda = 0) \sim 1/k_F$. Their ratio $l(\lambda = 0)/\xi(\lambda = 0) \sim \Delta_0/\epsilon_F$. For conventional superconductors [28], $l(\lambda = 0)/\xi(\lambda = 0) \sim 10^{-4}$, so they are well inside the BCS limit. The BCS mean-field theory works well; quantum and classical fluctuation effects can be neglected except very close to the critical transitions at finite temperatures. For high-temperature superconductors [29,31], $l(\lambda = 0)/\xi(\lambda = 0) \sim 10^{-1}$, so they are quite close to the BCS to BEC crossover, but still in the BCS limit with a well-defined Fermi surface. So quantum and classical fluctuation effects cannot be ignored [29]. In the BEC limit, they both get to the two-body bound-state size, and therefore $l(\lambda = 0)/\xi(\lambda = 0) \sim 1$. The results on $l$ in Eq. (29) at 3D and Eq. (38) show completely different behaviors from $\xi$. It is very instructive to compare the two different length scales. In the presence of SOC, on the BCS side, the coherence length $\xi_i(\lambda), i = x, y, z$ decreases monotonically and quickly moves into the BEC regime, so it can be used to characterize the BCS to BEC crossover quantitatively. Furthermore, it can be detected by a rf dissociation spectra experiment, while $l_i(\lambda)$ shows nonmonotonic behaviors and so it cannot be used to characterize the BCS to BEC crossover even qualitatively. Furthermore, it is not an experimentally measurable quantity.

In a future paper, we will compute the fluctuation corrections to the mean-field-theory results on the coherence length achieved in this paper. One can achieve the goal by calculating the fermion pairing correlation function given by Eq. (8) using the $1/N$ expansion [44,45]. It is known that the quantum fluctuation effects are important near the BCS to BEC regime. It may also be interesting to extend the zero-temperature results on the coherence length to finite temperatures, whose effects are especially important to 2D Rashba systems, studied in Secs. V and VI. However, it is not known how to extend the concepts of Cooper-pair size defined in Eq. (14) beyond mean-field results and to finite temperatures. Above all, its definition is based on the explicit form of the mean-field state. Therefore, the coherence length is a much more robust concept than the Cooper-pair size. It is also an experimentally measurable quantity through radio-frequency dissociation spectra. Of course, the two-body wave function is defined only for two fermions, and cannot be used to study a many-body system anyway. The Cooper-pair size has been evaluated at the mean field through the topological transition in [39]. As demonstrated in this paper, the coherence length shows quite different behaviors from the Cooper-pair size, and it may be useful to study the coherence length through various topological transitions driven by the Zeeman field [46–48].

## ACKNOWLEDGMENTS

We thank Fadi Sun for helpful discussions. Y.Y. and J.Y. are supported by NSF (DMR) under Grant No. 1161497, NSFC under Grant No. 11174210. W.L. is supported by the NKBRSFC under Grants No. 2011CB921502, No. 2012CB821305, NSFC under Grants No. 61227902, No. 61378017, No. 11434015, SKLQOQOD under Grant No. KF201403, and SPRPCAS under Grant No. XDB01020300.

[1] Jinwu Ye, Y. B. Kim, A. J. Millis, B. I. Shraiman, P. Majumdar, and Z. Tešanović, Phys. Rev. Lett. **83**, 3737 (1999).

[2] Lev P. Gor'kov and Emmanuel I. Rashba, Phys. Rev. Lett. **87**, 037004 (2001).

[3] Wang Yao and Qian Niu, Phys. Rev. Lett. **101**, 106401 (2008).

[4] Yu Chen, Jinwu Ye, and Guangshan Tian, J. Low Temp. Phys. **169**, 149 (2012).

[5] M. Z. Hasan and C. L. Kane, Rev. Mod. Phys. **82**, 3045 (2010).

[6] X. L. Qi and S. C. Zhang, Rev. Mod. Phys. **83**, 1057 (2011).

[7] For example, see "Exotic Phases of Frustrated Magnets" (KITP, Santa Barbara, 2012), http://online.kitp.ucsb.edu/online/fragnets-c12/.

[8] Y. J. Lin, K. Jiménez-García, and I. B. Spielman, Nature (London) **471**, 83 (2011).

[9] P. Wang, Z. Q. Yu, Z. Fu, J. Miao, L. Huang, S. Chai, H. Zhai, and J. Zhang, Phys. Rev. Lett. **109**, 095301 (2012).

[10] L. W. Cheuk, A. T. Sommer, Z. Hadzibabic, T. Yefsah, W. S. Bakr, and M. W. Zwierlein, Phys. Rev. Lett. **109**, 095302 (2012).

[11] For a review, see J. Dalibard, F. Gerbier, G. Juzeliūnas, and P. Öhberg, Rev. Mod. Phys. **83**, 1523 (2011).

[12] B. M. Anderson, I. B. Spielman, and G. Juzeliūnas, Phys. Rev. Lett. **111**, 125301 (2013).

[13] Z.-F. Xu, L. You, and M. Ueda, Phys. Rev. A **87**, 063634 (2013); Z.-F. Xu and L. You, *ibid.* **85**, 043605 (2012).

[14] J. P. Vyasanakere and V. B. Shenoy, Phys. Rev. B **83**, 094515 (2011)

[15] J. P. Vyasanakere, S. Zhang, and V. B. Shenoy, Phys. Rev. B **84**, 014512 (2011).

[16] Z.-Q. Yu and H. Zhai, Phys. Rev. Lett. **107**, 195305 (2011).

[17] H. Hu, L. Jiang, X. J. Liu, and H. Pu, Phys. Rev. Lett. **107**, 195304 (2011).

[18] Lianyi He and Xu-Guang Huang, Phys. Rev. Lett. **108**, 145302 (2012).

[19] Kezhao Zhou and Zhidong Zhang, Phys. Rev. Lett. **108**, 025301 (2012).

[20] Lianyi He and Xu-Guang Huang, Phys. Rev. B **86**, 014511 (2012).

[21] Jayantha P. Vyasanakere and Vijay B. Shenoy, Phys. Rev. A **86**, 053617 (2012).

[22] Shang-Shun Zhang, Xiao-Lu Yu, Jinwu Ye, and Wu-Ming Liu, Phys. Rev. A **87**, 063623 (2013).

[23] Shang-Shun Zhang, Jinwu Ye, and Wu-Ming Liu, arXiv:1403.7031.

[24] M. Aidelsburger, M. Atala, S. Nascimbène, S. Trotzky, Y.-A. Chen, and I. Bloch, Phys. Rev. Lett. **107**, 255301 (2011); J. Struck, C. Ölschläger, R. Le Targat, P. Soltan-Panahi, A. Eckardt, M. Lewenstein, P. Windpassinger, and K. Sengstock, Science **333**, 996 (2011); J. Struck, C. Ölschläger, M. Weinberg, P. Hauke, J. Simonet, A. Eckardt, M. Lewenstein, K. Sengstock, and P. Windpassinger, Phys. Rev. Lett. **108**, 225304 (2012); J. Struck, M. Weinberg, C. Ölschläger, P. Windpassinger, J. Simonet, K. Sengstock, R. Höppner, P. Hauke, A. Eckardt, M. Lewenstein, and L. Mathey, Nat. Phys. **9**, 738 (2013).

[25] M. Aidelsburger, M. Atala, M. Lohse, J. T. Barreiro, B. Paredes, and I. Bloch, Phys. Rev. Lett. **111**, 185301 (2013); H. Miyake, G. A. Siviloglou, C. J. Kennedy, W. C. Burton, and W. Ketterle, *ibid.* **111**, 185302 (2013); C. J. Kennedy, G. A. Siviloglou, H. Miyake, W. C. Burton, and W. Ketterle, *ibid.* **111**, 225301 (2013).

[26] Fadi Sun, Xiao-Lu Yu, Jinwu Ye, Heng Fan, and Wu-Ming Liu, Sci. Rep. **3**, 2119 (2013).

[27] Fa-Di Sun, Jinwu Ye, and W. M. Liu, arXiv:1408.3399.

[28] P. G. De Gennes, *Superconductivity of Metals and Alloys* (Perseus, New York, 1999). On page 96, Eq. (14) was evaluated with respect to a two-fermion wave function outside a Fermi surface, which is the original Cooper-pair problem. Due to the absence of the Fermi surface, this two-body bound state discussed in [14] still differs from the original Cooper-pair problem.

[29] A. J. Leggett, *Quantum Liquids* (Oxford University Press, Oxford, 2006).

[30] Immanuel Bloch, Jean Dalibard, and Wilhelm Zwerger, Rev. Mod. Phys. **80**, 885 (2008).

[31] Jinwu Ye, Phys. Rev. Lett. **86**, 316 (2001); **87**, 227003 (2001); Phys. Rev. B. **65**, 214505 (2002).

[32] Jinwu Ye, T. Shi, and Longhua Jiang, Phys. Rev. Lett. **103**, 177401 (2009);

[33] T. Shi, Longhua Jiang, and Jinwu Ye, Phys. Rev. B **81**, 235402 (2010)

[34] Jinwu Ye, Fadi Sun, Yi-Xiang Yu, and Wuming Liu, Ann. Phys. **329**, 51 (2013).

[35] Jinwu Ye, J. Low Temp. Phys. **158**, 882 (2010).

[36] As shown in Sec. II B, the reason for quotation marks on both the "Cooper-pair wave function" and "Cooper-pair size" is that they are not really physical, so they may not be really understood as the Cooper-pair wave function and Cooper-pair size. For illustration purposes, they are evaluated here to compare with the physical coherence length and two-body bound state. Furthermore, several authors [16, 39] also evaluated this unphysical length in different contexts. For notational simplicity, we dropped the quotation mark in the following.

[37] J. R. Engelbrecht, M. Randeria, and C. A. R. Sá de Melo, Phys. Rev. B **55**, 15153 (1997).

[38] Christian H. Schunck, Yong-il Shin, Andr Schirotzek, and Wolfgang Ketterle, Nature (London) **454**, 739 (2008).

[39] N. Read and Dmitry Green, Phys. Rev. B **61**, 10267 (2000). For the purpose of making connections with the $p$-wave pairing nature of the non-Abelian Pfaffian fractional quantum Hall effect (FQHE) wave function, the "Cooper-pair wave function" $g(\vec{r})$ is the suitable quantity to compare.

[40] Note that $\xi = \sqrt{\xi_x^2 + \xi_y^2 + \xi_z^2} = \frac{a_s}{\sqrt{2}}$, which is exactly the size of the two-body bound state in Eq. (31).

[41] In Ref. [16], only the $l_i$ at the resonance $1/k_F a_s = 0$ was calculated. Our curve in Fig. 4 at the resonance recovers their results. But, as indicated in the text, the nonmonotonic behaviors of $l_i$ discovered in Fig. 4 can only be seen in the BCS side, $a_s < 0$. Of course, as indicated in the text, the $l_i$ cannot be used to characterize the BCS to BEC crossover and is not an experimentally measurable quantity anyway.

[42] M. Randeria, J.-M. Duan, and L.-Y. Shieh, Phys. Rev. B **41**, 327 (1990).

[43] V. M. Loktev, R. M. Quick, and S. G. Sharapov, Phys. Rep. **349**, 1 (2001).

[44] Jinwu Ye and C. L. Zhang, Phys. Rev. A **84**, 023840 (2011).

[45] Yu Yi-Xiang, Jinwu Ye, and Wu-Ming Liu, Sci. Rep. **3**, 3476 (2013).
[46] Masatoshi Sato, Yoshiro Takahashi, and Satoshi Fujimoto, Phys. Rev. Lett. **103**, 020401 (2009).
[47] Ming Gong, Sumanta Tewari, and Chuanwei Zhang, Phys. Rev. Lett. **107**, 195303 (2011).
[48] Xuebing Luo, K. Zhou, W. Liu, Z. Liang, and Z. Zhang, Phys. Rev. A **89**, 043612 (2014).